An Adaptive MDS-coded OFDM Waveform for Low-Altitude ISAC: Design and Optimization

Yiqian Huang, Gang Wu, *Senior Member, IEEE*, Ping Yang, *Senior Member, IEEE*, Zilong Liu, *Senior Member, IEEE*, Yue Xiao, *Member, IEEE*, Tony Q. S. Quek, *Fellow, IEEE*

***Abstract*—The low-altitude economy (LAE), an emerging economic paradigm encompassing various flight activities in low-altitude airspace, has attracted widespread attention from academia and industry due to its appealing economic and social benefits. In this paper, we investigate the design of integrated sensing and communication (ISAC) waveforms for LAE applications. Specifically, we propose an adaptive ISAC waveform, which integrates the maximum distance separable (MDS) code and index modulation (IM) into the orthogonal frequency division multiplexing (OFDM) waveform, namely A-MDS-OFDM-IM. This design combines the hybrid benefits of MDS code, IM, and OFDM techniques, i.e., the error detection capability of MDS code, the high spectral efficiency (SE) of IM, and the high sensing resolution of OFDM, thereby enabling robust communication and sensing. A comprehensive performance analysis of A-MDS-OFDM-IM is provided, including its bit error rate (BER), peak-to-sidelobe level (PSL), and peak-to-average power ratio (PAPR). Moreover, to address the high PAPR issue of A-MDS-OFDM-IM, we develop an adaptive design criterion based on the alternating direction method of multipliers (ADMM), which is capable of jointly optimizing the communication, sensing, and PAPR performance of the proposed system. Simulation results demonstrate that the proposed waveform achieves better BER performance than conventional OFDM-based waveforms under a non-ideal high power amplifier (HPA), owing to its low-PAPR characteristic. Additionally, the proposed waveform ensures robust sensing with satisfactory PSL performance, making it a promising ISAC waveform for LAE applications.**

***Index Terms*—Adaptive waveform design, alternating direction method of multipliers (ADMM), integrated sensing and communication (ISAC), low-altitude economy (LAE), orthogonal frequency division multiplexing (OFDM).**

I. Introduction

As an emerging economic paradigm integrating advanced technologies across fields such as next-generation communications and automation, the low-altitude economy (LAE) has attracted increasing attention from both academia and industry [1]–[3]. Driven by advancements in the unmanned aerial vehicle (UAV) industry, LAE encompasses a variety of aerial activities within the airspace below 1,000 meters, creating both commercial and societal values [4]. Due to its cost and deployment efficiency, LAE is anticipated to revolutionize a number of vertical industries, including transportation [5], delivery [6], and agriculture [7].

Y. Huang, G. Wu, P. Yang and Y. Xiao are with the National Key Laboratory of Wireless Communications, University of Electronic Science and Technology of China, 611731, Sichuan, China. (e-mail: yqhuang@std.uestc.edu.cn, wugang99@uestc.edu.cn, yang.ping@uestc.edu.cn, xiaoyue@uestc.edu.cn).

Zilong Liu is with the School of Computer Science and Electronics Engineering, University of Essex, Colchester, Surrey CO4 3SQ, U.K. (e-mail: zilong.liu@essex.ac.uk).

Tony Q. S. Quek is with the Information Systems Technology and Design Pillar, Singapore University of Technology and Design, Singapore, 487372. (e-mail: tonyquek@sutd.edu.sg).

The corresponding author is Ping Yang.

To support the diverse applications in LAE, it is crucial to enhance the spectral and hardware efficiencies of low-altitude systems, whilst ensuring the safety of authorized aircraft [8], [9]. In this context, the integrated sensing and communication (ISAC) technology has emerged as a promising solution for addressing these challenges [10]–[12]. Specifically, by combining communication and sensing functionalities into a unified hardware platform, ISAC facilitates the efficient utilization of both spectral and hardware resources [13], [14]. Moreover, ISAC enables aircraft to simultaneously provide communication services for authorized users, while performing sensing operations to detect unauthorized targets, thereby improving overall safety [15].

In ISAC systems, a key challenge is the design of integrated waveforms that concurrently support reliable communication and sensing [16]–[18]. Among the existing waveforms, orthogonal frequency division multiplexing (OFDM), a standard waveform of the fifth generation (5G) mobile communication networks, is recognized as a competitive candidate due to its efficient hardware implementation and robustness to interference [19], [20]. To date, extensive research has demonstrated the feasibility and effectiveness of OFDM in various ISAC scenarios [21]–[23]. More importantly, Liu *et al.* proved that OFDM is the optimal communication-centric ISAC waveform for ranging, further highlighting its potential for ISAC applications [24]. Motivated by the appealing advantages of OFDM, several OFDM-based ISAC waveforms were proposed in recent years [18], [25], [26]. For instance, [25] proposed an adaptive OFDM waveform based on power allocation, attaining a trade-off between the data rate and peak-to-sidelobe level (PSL). In [26], a probabilistic constellation-shaped OFDM waveform was developed to reduce the sidelobes of the ambiguity function, at the expense of a reduced data rate. Moreover, [27] and [28] exploited the use of OFDM with index modulation (OFDM-IM) in ISAC systems, where only a subset of subcarriers are activated, and their locations carry extra information. As shown in previous research of [29] and [30], OFDM-IM exhibits improved bit error rate (BER) performance over conventional OFDM, but it further confronts challenges in reduced sensing performance [27]. By collecting the observations of multiple receive signals [31] or preprocessing the transmit signals [32], the sensing performance of OFDM-IM can be improved with an increase in system complexity. Recently, a pair of maximum distance separable (MDS) coded OFDM (MDS-OFDM) waveforms were proposed in [33]. Thanks to the increased minimum Hamming distance enabled by the MDS code, MDS-OFDM yields improved BER performance compared to OFDM-IM [33], [34]. The application of MDS-OFDM in ISAC systems was discussed in [35], which demonstrates an excellent sensing performance. Due to its high communication reliability and

robust sensing exhibited in [33]–[35], MDS-OFDM may serve as a promising ISAC waveform for LAE applications.

Despite the potential of MDS-OFDM for both communications and sensing, it inherits the high peak-to-average power ratio (PAPR) problem from classical OFDM [36]. It is known that a high PAPR may lead to distorted transmit signals when passing through a high power amplifier (HPA), resulting in degradation in both communication and sensing performance [37], [38]. Therefore, it is necessary to reduce the PAPR of MDS-OFDM to ensure its effectiveness in LAE applications. Recent studies have addressed the high-PAPR problem in OFDM-based ISAC waveforms [39], [40]. For example, Golay complementary sequences and tone reservation technology were adopted in [41] and [42] to solve the high-PAPR problem, respectively. In [43], power allocation strategies were investigated to optimize the sensing performance under a PAPR constraint. Additionally, [44] developed a generalized OFDM-based ISAC waveform structure, where the communication sub-bands are arbitrarily located within a large contiguous radar frequency band. In this framework, PAPR reduction can be achieved by optimizing the frequency-domain (FD) signals in the radar sub-bands [44]–[47]. While these methods can effectively reduce the PAPRs of OFDM-based waveforms, they may result in reduced transmission rate and spectral efficiency (SE). Given that the MDS code may also cause additional spectral overhead, these PAPR-reduction techniques may not be ideal for MDS-OFDM. Thus, further exploration of low-PAPR MDS-OFDM waveform design is essential for ensuring reliable communication and sensing in LAE applications.

In this paper, an adaptive OFDM-based ISAC waveform is developed for LAE applications by integrating the concept of IM with MDS-OFDM, which demonstrates considerably reduced PAPR compared to conventional OFDM-based waveforms with a satisfactory SE. The main contributions of this paper are summarized as follows:

1) We propose an adaptive OFDM-based ISAC waveform, termed A-MDS-OFDM-IM, which simultaneously achieves robust communication and sensing in LAE scenarios. Specifically, the proposed waveform divides the subcarriers into two types of subcarrier groups (SGs), namely modulation subcarrier groups (MSGs) and optimization subcarrier groups (OSGs). The MSGs are generated using a simple MDS-coded in-phase and quadrature modulation (MDS-IQM) scheme to ensure reliable communication, and the OSGs are adaptively designed for waveform optimization. It is worth emphasizing that the locations of OSGs are used to convey extra information, thereby enhancing the SE.
2) With the proposed waveform, a UAV-assisted ISAC system is designed, and the theoretical analysis of the system's BER, PSL, and PAPR is provided. Using these theoretical results, we develop an adaptive design criterion that jointly optimizes the system's BER, PSL, and PAPR. Specifically, BER and PSL are optimized by a search-based method and a carefully designed convex optimization algorithm, respectively. While PAPR is minimized by an alternating direction method of multipliers (ADMM)-based algorithm, which shows rapid and stable convergence.
3) Numerical simulations are conducted to demonstrate the effectiveness of A-MDS-OFDM-IM for LAE applications. Moreover, the trade-off between the communication and sensing performance of A-MDS-OFDM-IM, as well as the convergence performance of the proposed ADMM-based algorithm, are also evaluated.

The remainder of this paper is organized as follows. In Section II, we introduce the proposed ISAC model based on the A-MDS-OFDM-IM waveform, including the waveform design and the communication and sensing signal models. Section III provides the theoretical results of the system's BER, PSL, and PAPR, and Section IV discusses the adaptive design criterion. Numerical results are presented in Section V, and Section VI summarizes this paper.

Notations

The following notations will be used throughout this paper.

— x, $\mathbf{x}$, $\mathbf{X}$, and $\mathcal{X}$ denote a scalar, a vector, a matrix, and a set, respectively.

— $x(m)$ and $\mathcal{X}(m)$ denote the m-th element of $\mathbf{x}$ and $\mathcal{X}$, respectively. $\mathbf{X}_m$ and $X(m,n)$ denote the m-th column and (m,n)-th element of $\mathbf{X}$, respectively.

— $\mathbf{I}_N$ denotes the N-dimensional unit diagonal matrix, and $\mathbf{0}_N$ denotes the N-dimensional zero matrix.

— $\mathrm{diag}[\mathbf{x}]$ denotes a diagonal matrix with the diagonal vector of $\mathbf{x}$.

— $\mathbb{C}^{M\times N}$, $\mathbb{R}^{M\times N}$, and $\mathbb{B}^{M\times N}$ denote the sets of $(M\times N)$-dimensional complex-valued, real-valued, and binary matrices, respectively.

— $|\mathbf{x}| = [|x(1)|, |x(2)|, \ldots, |x(N)|]^T$ denotes the element-wise modulus of $\mathbf{x}$, and $|\mathbf{x}|^2 = [|x(1)|^2, |x(2)|^2, \ldots, |x(N)|^2]^T$ denotes the power spectrum of $\mathbf{x}$, assuming that $\mathbf{x}$ is an N-dimensional column vector.

— $\|\mathbf{x}\|_F$ and $\|\mathbf{x}\|_\infty$ denote the Frobenius norm and infinite norm of $\mathbf{x}$, respectively.

— $\mathcal{X}\backslash x$ removes the element x from the set $\mathcal{X}$.

— $\mathrm{E}(\cdot)$ and $\mathrm{Var}(\cdot)$ denote the mean and variance operators, respectively.

— mod denotes the modulo operator.

— $\mathrm{Re}(\cdot)$ and $\mathrm{Im}(\cdot)$ denote the real part and imaginary part operators, respectively.

— $\lfloor\cdot\rfloor$ denotes the round down operator.

— $(\cdot)^{-1}$, $(\cdot)^T$, $(\cdot)^*$, and $(\cdot)^H$ denote the inverse, transpose, conjugate, and conjugate transpose operators, respectively.

— $\mathcal{CN}(u,\sigma^2)$ denotes the distribution of a circularly symmetric complex-valued Gaussian random variable with mean u and variance σ^2.

— $j=\sqrt{-1}$ is the imaginary unit.

— $Q(x)=\frac{1}{\sqrt{2\pi}}\int_x^\infty e^{\frac{t^2}{2}}dt$ is the Q-function.

— $C(n,k)=\frac{n!}{(n-k)!k!}$ is the binomial coefficient.

— In the proposed A-MDS-OFDM-IM waveform, variables correlated with MSGs and OSGs are labeled with superscripts 'm' and 'o', respectively.

— In the MDS-IQM scheme, variables correlated with the I- and Q-branches are labeled with superscripts 'i' and 'q', respectively.

— In the proposed ISAC model, the communication and sensing signals are distinguished by superscripts 'c' and 's', respectively.

II. System Model

As depicted in Fig. 1, we consider a UAV-empowered mono-static ISAC system operating in low-altitude airspace,

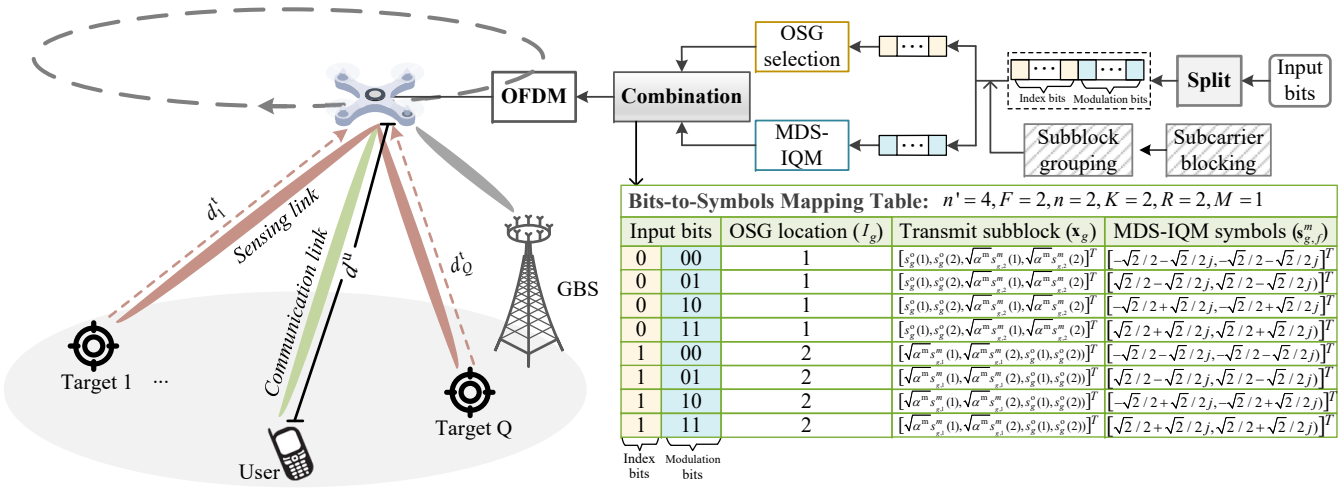

Fig. 1. Low-altitude mono-static ISAC model based on the proposed MDS-OFDM-IM waveform.

where a ground base station (GBS) is employed to control the network. In this framework, a UAV simultaneously provides communication services to the user and performs sensing tasks for unauthorized targets, utilizing the same waveform for both functions. Specifically, communication information is embedded in the transmit A-MDS-OFDM-IM waveforms, while the UAV executes sensing operations based on the echoes. The model assumes that both the UAV and user are equipped with a single antenna, with the distance between them represented by d^{u}. Additionally, the UAV is assumed to fly at a fixed height with a constant velocity.

A. A-MDS-OFDM-IM Waveform Design

In the A-MDS-OFDM-IM transmitter, an OFDM symbol with N subcarriers is first divided into G subcarrier blocks (SBs), each containing $n' = N/G$ subcarriers. Then, the n' subcarriers within an SB are partitioned into F SGs, yielding $n = n'/F$ subcarriers per group. Specifically, let us denote the FD transmit signal frame of the g-th SB as

$$\mathbf{x}_g = \left[\mathbf{x}_{g,1}^T, \mathbf{x}_{g,2}^T, \ldots, \mathbf{x}_{g,F}^T\right]^T, \ g \in \{1, 2, \ldots, G\}, \quad (1)$$

where $\mathbf{x}_{g,f} \in \mathbb{C}^{n\times 1}$ represents the FD signal stream of the f-th SG in $\mathbf{x}_g$, $f \in \{1, 2, \ldots, F\}$. Using (1), the entire FD transmit frame $\mathbf{x} \in \mathbb{C}^{N\times 1}$ is given by

$$\mathbf{x} = [x(0), x(1), \ldots, x(N-1)]^T = \left[\mathbf{x}_1^T, \mathbf{x}_2^T, \ldots, \mathbf{x}_G^T\right]^T. \quad (2)$$

Furthermore, the F SGs within each SB are classified into two types: one OSG and $F-1$ MSGs. Let I_g denote the location of OSG in $\mathbf{x}_g$, then the FD signal stream of the f-th SG in $\mathbf{x}_g$, i.e., $\mathbf{x}_{g,f}$, can be formulated as

$$\mathbf{x}_{g,f} = \begin{cases} \sqrt{\alpha^{\mathrm{m}}}\mathbf{s}^{\mathrm{m}}_{g,f}, & f \neq I_g, \\ \mathbf{s}^{\mathrm{o}}_{g}, & f = I_g, \end{cases} \quad g = 1, 2, \ldots, G, \ f = 1, 2, \ldots, F, \quad (3)$$

with

$$\alpha^{\mathrm{m}} = \frac{N - \sum_{g=1}^{G} \|\mathbf{s}^{\mathrm{o}}_g\|_F^2}{G(F-1)}. \quad (4)$$

Here, $\mathbf{s}^{\mathrm{m}}_{g,f} \in \mathbb{C}^{n\times 1}$ denotes the signal stream of MSG $\mathbf{x}_{g,f}$, which is generated by a simple MDS-IQM scheme [33]. $\mathbf{s}^{\mathrm{o}}_g \in \mathbb{C}^{n\times 1}$ represents the FD signal stream of OSG in $\mathbf{x}_g$, whose signals are adaptively designed for waveform optimization. α^{m} is the average power of the FD MSGs, which is used for the normalization of $\mathrm{E}(\|\mathbf{x}\|_F^2) = N$. Recall that the subscripts 'm' and 'o' distinguish variables related to MSGs and OSGs, respectively.

A total of L information bits entering the A-MDS-OFDM-IM transmitter are distributed across the G SBs, with each SB conveying $l = L/G$ bits. As shown in Fig. 1, unlike conventional OFDM, the l information bits for an SB are further divided into two types, with l^{o} index bits and $(F-1)l^{\mathrm{m}}$ modulation bits, i.e., $l = l^{\mathrm{o}} + (F-1)l^{\mathrm{m}}$. Here, $l^{\mathrm{o}} = \log_2 F$ index bits are used to determine the location of the OSG in the corresponding SB. The remaining $(F-1)l^{\mathrm{m}}$ bits determine the FD signals of the $F-1$ MSGs, with each MSG conveying l^{m} information bits. Specifically, denoted by $\mathbf{b}_g \in \mathbb{B}^{l^{\mathrm{o}}\times 1}$ the index bits for the g-th SB, the location of the g-th OSG is calculated by converting $\mathbf{b}_g$ to its decimal representation, i.e.,

$$I_g = \sum_{l'=1}^{l^{\mathrm{o}}} 2^{l'-1} b_g(l') + 1, \ g \in \{1, 2, \ldots, G\}. \quad (5)$$

Once the locations of G OSGs are obtained, we can proceed with the generation of MDSs and OSGs, respectively.

1) Generation of MSGs by MDS-IQM: To begin with, let us denote the modulation orders for the I- and Q-branches as K and R, respectively. In MDS-IQM, we first generate a total of K disjoint M-ary pulse amplitude modulation (PAM) constellations $\{\mathcal{S}_1^{\mathrm{i}}, \mathcal{S}_2^{\mathrm{i}}, \ldots, \mathcal{S}_K^{\mathrm{i}}\}$ for I-branch modulation. These constellations are obtained by first generating a KM-ary PAM constellation $\mathcal{S}$ with a normalized power of 1/2, and then grouping every M points in $\mathcal{S}$ with an index interval of K into a new constellation. In this way, the k-th M-ary PAM constellation is given by

$$\mathcal{S}_k^{\mathrm{i}} = \{\mathcal{S}(k), \mathcal{S}(k+K), \ldots, \mathcal{S}(k+K(M-1))\}, \ k \in \{1, 2, \ldots, K\}. \quad (6)$$

Similarly, R disjoint M-ary PAM constellations $\{\mathcal{S}_1^{\mathrm{q}}, \mathcal{S}_2^{\mathrm{q}}, \ldots, \mathcal{S}_R^{\mathrm{q}}\}$ are created for the Q-branch modulation.

When the constellations $\{\mathcal{S}_1^{\mathrm{i}}, \mathcal{S}_2^{\mathrm{i}}, \ldots, \mathcal{S}_K^{\mathrm{i}}\}$ and $\{\mathcal{S}_1^{\mathrm{q}}, \mathcal{S}_2^{\mathrm{q}}, \ldots, \mathcal{S}_R^{\mathrm{q}}\}$ are established, identical modulation procedures are then applied to each MSG. Hence, we now focus on generating one MSG to introduce the MDS-IQM scheme and omit its block and group index. Specifically, in MDS-IQM, l^{m} bits conveyed by an MSG are first split into two parts, with l^{i} bits for I-branch modulation and l^{q} bits for Q-branch modulation, respectively. Subsequently, l^{i} and l^{q}

bits are divided into two parts as

$$\begin{cases} l^{\mathrm{i}} = l_1^{\mathrm{i}} + l_2^{\mathrm{i}} = (n-1)\log_2 K + n\log_2 M \\ l^{\mathrm{q}} = l_1^{\mathrm{q}} + l_2^{\mathrm{q}} = (n-1)\log_2 R + n\log_2 M, \end{cases} \tag{7}$$

leading to

$$l^{\mathrm{m}} = l^{\mathrm{i}} + l^{\mathrm{q}} = (n-1)\log_2 KR + 2n\log_2 M. \tag{8}$$

In (7), l_1^{i} and l_1^{q} bits are used to select one constellation for each subcarrier from the K and R disjoint constellations, respectively. l_2^{i} and l_2^{q} bits determine the I- and Q-components of each subcarrier by selecting one symbol from the chosen constellation, respectively.

More specifically, in MDS-IQM, a simple mapping rule is first employed to map l_1^{i} and l_1^{q} bits into two n-dimensional tuples of MDS codes, which can increase the minimum Hamming distance between modulation symbols. To introduce this mapping rule, let us denote the two obtained MDS codes as $\mathbf{c}^{\mathrm{i}}$ and $\mathbf{c}^{\mathrm{q}}$, respectively. The first $n-1$ codewords of $\mathbf{c}^{\mathrm{i}}$ and $\mathbf{c}^{\mathrm{q}}$ are acquired by converting every $\log_2 K$ bits of l_1^{i} and $\log_2 R$ bits of l_1^{q} into their decimal representations, respectively. The n-th codewords of $\mathbf{c}^{\mathrm{i}}$ and $\mathbf{c}^{\mathrm{q}}$ are determined by their first $n-1$ codewords, satisfying

$$\begin{cases} c^{\mathrm{i}}(n) = K - (c^{\mathrm{i}}(1) + c^{\mathrm{i}}(2) + \cdots + c^{\mathrm{i}}(n-1)) \bmod K \\ c^{\mathrm{q}}(n) = R - (c^{\mathrm{q}}(1) + c^{\mathrm{q}}(2) + \cdots + c^{\mathrm{q}}(n-1)) \bmod R. \end{cases} \tag{9}$$

Based on $\mathbf{c}^{\mathrm{i}}$ and $\mathbf{c}^{\mathrm{q}}$, the constellations for the I- and Q-branches of the a-th subcarrier are selected as $\mathcal{S}^{\mathrm{i}}_{c^{\mathrm{i}}(a)}$ and $\mathcal{S}^{\mathrm{q}}_{c^{\mathrm{q}}(a)}$, respectively, with $a \in \{1, 2, \ldots, n\}$.

Subsequently, we convert every $\log_2 M$ bits of l_2^{i} and l_2^{q} into their decimal representations, which are used to determine the I- and Q-components of the n subcarriers. Let us denote the resulting n-dimensional vectors corresponding to l_2^{i} and l_2^{q} bits as $\mathbf{d}^{\mathrm{i}} \in \mathbb{C}^{n\times 1}$ and $\mathbf{d}^{\mathrm{q}} \in \mathbb{C}^{n\times 1}$, respectively, then the I- and Q-components of an MSG, denoted by $\mathbf{s}^{\mathrm{i}} \in \mathbb{C}^{n\times 1}$ and $\mathbf{s}^{\mathrm{q}} \in \mathbb{C}^{n\times 1}$, are given by

$$\begin{cases} s^{\mathrm{i}}(a) = \mathcal{S}^{\mathrm{i}}_{c^{\mathrm{i}}(a)}(d^{\mathrm{i}}(a)), \\ s^{\mathrm{q}}(a) = \mathcal{S}^{\mathrm{q}}_{c^{\mathrm{q}}(a)}(d^{\mathrm{q}}(a)), \end{cases} \quad a = 1, 2, \ldots, n. \tag{10}$$

Based on (10), the FD signal stream of an MSG, denoted by $\mathbf{s}^{\mathrm{m}} \in \mathbb{C}^{n\times 1}$, is finally given by

$$s^{\mathrm{m}}(a) = s^{\mathrm{i}}(a) + j s^{\mathrm{q}}(a),\ a = 1, 2, \ldots, n. \tag{11}$$

2) Generation of OSGs: When the FD signals of all $G(F-1)$ MSGs are obtained, the FD signals of G OSGs are adaptively designed based on them to jointly optimize the system's BER, PSL, and PAPR. The adaptive design of OSGs is detailed in Section IV.

Furthermore, the A-MDS-OFDM-IM transmitter imposes a power constraint on the OSGs, fixing their power to a constant α^{o} that exceeds the maximum power of an MSG. The value of α^{o} is subject to optimization. Specifically, let $\mathcal{A}^{\mathrm{m}}$ be the set of all possible transmit powers of an MSG generated by MDS-IQM. Based on the concept of MDS-IQM, the cardinality of $\mathcal{A}^{\mathrm{m}}$ is $|\mathcal{A}^{\mathrm{m}}| = (KR)^{n-1}M^{2n} \triangleq \Lambda^{\mathrm{m}}$, which also corresponds to the number of legitimate FD signal streams of an MSG. By sorting the elements of $\mathcal{A}^{\mathrm{m}}$ in descending order, i.e., $\mathcal{A}^{\mathrm{m}}(1) \geq \mathcal{A}^{\mathrm{m}}(2) \geq \cdots \geq \mathcal{A}^{\mathrm{m}}(\Lambda^{\mathrm{m}})$, the power constraint on OSGs is expressed as

$$\|\mathbf{s}_g^{\mathrm{o}}\|_F^2 = \alpha^{\mathrm{o}} > \mathcal{A}^{\mathrm{m}}(1),\ g = 1, 2, \ldots, G. \tag{12}$$

This constraint enables the communication receiver to recover index information through straightforward power comparisons, thereby avoiding the necessity to convey the FD signals of OSGs as side information. Based on (12), the average power of the FD MSGs, as defined in (4), is given by

$$\alpha^{\mathrm{m}} = \frac{N - G\alpha^{\mathrm{o}}}{G(F-1)}. \tag{13}$$

Upon acquiring the FD transmit signal stream $\mathbf{x}$, OFDM operations are conducted on $\mathbf{x}$ to generate the baseband discrete time domain (TD) signal stream. Specifically, an N-dimensional inverse fast Fourier transform (IFFT) is first performed on $\mathbf{x}$ to generate the discrete TD transmit signal stream $\mathbf{x}'$. Then, a cyclic prefix (CP) is added to $\mathbf{x}'$. Finally, after radio frequency (RF) operations including up-conversion, amplification, and digital-to-analog conversion, the TD signal stream is sent out.

For ease of understanding, Fig. 1 presents an example to illustrate the generation for an SB with $n' = 4, F = 2, n = 2, K = 2, R = 2$, and $M = 1$. In this example, an SB with 4 subcarriers is divided into two SGs, and a total of three information bits are conveyed by each SB. The first bit selects one OSG from the two SGs, and the remaining two bits determine the FD signals of the MSG. For example, considering the input bits '000'. Its first bit '0' selects the first SG as the OSG based on (5). The second SG is the MSG, whose FD signal stream is generated by the MDS-IQM scheme in Section II-A, which is $[-\sqrt{2}/2 - \sqrt{2}/2j, -\sqrt{2}/2 - \sqrt{2}/2j]^T$.

B. Communication Signal Model

Due to the relatively high altitude of the UAV, the communication link between the UAV and user is generally dominated by the line-of-sight (LoS) component with path loss effect $\beta = \xi\lambda^2/4\pi(d^{\mathrm{u}})^2$, where ξ and λ represent the antenna gain and wavelength, respectively [9], [11], [15], [20]. Given that the UAV can be treated as quasi-static during a short time interval, it is reasonable to assume that the path loss remains constant within an OFDM symbol.

At the user side, after the RF operations and CP removal, the receive discrete TD signal stream is converted to the FD through FFT. Specifically, the FD receive signal stream $\mathbf{y}^{\mathrm{c}} \in \mathbb{C}^{N\times 1}$ is given by

$$\mathbf{y}^{\mathrm{c}} = \sqrt{\beta}\mathbf{x} + \mathbf{z}, \tag{14}$$

where $\mathbf{z} \sim \mathcal{CN}(0, \sigma^2)$ represents the additive white Gaussian noise (AWGN). Then, the subcarriers of $\mathbf{y}^{\mathrm{c}}$ are organized in the same manner as those of $\mathbf{x}$, so that $\mathbf{y}^{\mathrm{c}}$ can be expressed as $\mathbf{y}^{\mathrm{c}} = [(\mathbf{y}_1^{\mathrm{c}})^T, (\mathbf{y}_2^{\mathrm{c}})^T, \ldots, (\mathbf{y}_G^{\mathrm{c}})^T]^T$, with $\mathbf{y}_g^{\mathrm{c}} = [(\mathbf{y}_{g,1}^{\mathrm{c}})^T, (\mathbf{y}_{g,2}^{\mathrm{c}})^T, \ldots, (\mathbf{y}_{g,F}^{\mathrm{c}})^T]^T \in \mathbb{C}^{n\times 1}$.

Based on the receive signal model in (14), signal detection techniques are then employed to estimate $\mathbf{x}$ of (2) from $\mathbf{y}^{\mathrm{c}}$. Considering the side information-free transmission and assuming that β is known at the receiver, we propose a simple decoupled detector for each SB of $\mathbf{y}^{\mathrm{c}}$ in (15) and (16). Specifically, the index information is identified as the location of the SG with the maximum power in each SB, while the modulation signals are recovered by performing the maximum likelihood (ML) detection on the remaining SGs.

$$\hat{I}_g = \underset{1\leq f\leq F}{\operatorname{argmax}} \|\mathbf{y}_{g,f}^{\mathrm{c}}\|_F^2,\ g \in \{1, 2, \ldots, G\}, \tag{15}$$

$$\hat{\mathbf{x}}_{g,f} = \underset{\mathbf{s} \in \mathcal{S}^{\mathrm{m}}}{\operatorname{argmin}} \|\mathbf{y}^{\mathrm{c}}_{g,f} - \sqrt{\beta\alpha^{\mathrm{m}}}\mathbf{s}\|_F^2, \ f \in \{1,2,\ldots,F\} \backslash \hat{I}_g. \quad (16)$$

Here, $\hat{I}_g$ denotes the location of the detected OSG, and $\hat{\mathbf{x}}_{g,f} \in \mathbb{C}^{n\times 1}$ represents the detected signal stream for the f-th SG in the g-th SB. The set $\mathcal{S}^{\mathrm{m}}$ comprises all valid combinations of MDS-IQM signals for an MSG, and $\mathbf{s} \in \mathbb{C}^{n\times 1}$ is one combination in $\mathcal{S}^{\mathrm{m}}$. Note that the cardinality of $\mathcal{S}^{\mathrm{m}}$ is the same as that of $\mathcal{A}^{\mathrm{m}}$ defined in Section II-A, i.e., $|\mathcal{S}^{\mathrm{m}}| = |\mathcal{A}^{\mathrm{m}}| = \Lambda^{\mathrm{m}}$. As can be seen from (15) and (16), our proposed detector effectively achieves the detection of index information and modulation signals without the knowledge of transmit signals on OSGs.

C. Sensing Signal Model

In the sensing stage, as shown in Fig. 1, let us assume that the transmit A-MDS-OFDM-IM waveform is reflected by Q targets with distances $\{d_1^{\mathrm{t}}, d_2^{\mathrm{t}}, \ldots, d_Q^{\mathrm{t}}\}$, then the FD receive echo at the UAV, denoted by $\mathbf{y}^{\mathrm{s}} = [y^{\mathrm{s}}(1), y^{\mathrm{s}}(2), \ldots, y^{\mathrm{s}}(N)]^T \in \mathbb{C}^{N\times 1}$, is given by

$$y^{\mathrm{s}}(i) = \sum_{q=1}^{Q} \gamma_q x(i) e^{-j2\pi i \tau_q \Delta f} + z(i), \ i = 0,1,\ldots,N-1, \quad (17)$$

where

$$\gamma_q = \frac{c^2 \varsigma_q}{f_{\mathrm{c}}^2 (4\pi)^3 (d_q^{\mathrm{t}})^3}, \ q \in \{1,2,\ldots,Q\}, \quad (18)$$

is the attenuation induced by the propagation and scattering processes associated with the q-th target, ς_q is the radar cross-section of the q-th target, c is the speed of light, f_c is the carrier frequency, $\tau_q = 2d_q^{\mathrm{t}}/c$ is the round-trip time delay of the q-th target, and Δf is the subcarrier spacing.

Utilizing the sensing signal model in (17), an FFT-based algorithm in [16] is then adopted to estimate the ranges of the Q targets. Specifically, given that the UAV knows the transmit waveform $\mathbf{x}$, the ranges of the Q targets are estimated by performing an N-dimensional IFFT on the Hadamard product of $\mathbf{y}^{\mathrm{s}}$ and the conjugate of $\mathbf{x}$.

III. Performance Analysis

In this section, we analyze the BER, PSL, and PAPR of the proposed A-MDS-OFDM-IM waveform.

A. BER of the Proposed A-MDS-OFDM-IM

As shown in Fig. 1, in the proposed A-MDS-OFDM-IM waveform, identical procedures are applied to each SB, resulting in a uniform average BER for all SBs. Thus, we now focus on deriving the average BER for a single SB, defined as the ratio of the average number of erroneous bits $\tilde{l}$ to the total number of transmit bits l. Specifically, erroneous bits in an SB arise from two types of errors, namely index bit errors and modulation bit errors. Using this relationship, the average BER of the proposed A-MDS-OFDM-IM waveform can be expressed as

$$\mathrm{BER} = \frac{\tilde{l}}{l} = \frac{\tilde{l}^{\mathrm{o}} + \tilde{l}^{\mathrm{m}}}{l}, \quad (19)$$

where $\tilde{l}^{\mathrm{o}}$ and $\tilde{l}^{\mathrm{m}}$ denote the average numbers of erroneous index bits and modulation bits in an SB, respectively.

1) Average Number of Erroneous Index Bits: For an SB, erroneous index bits arise when the location of OSG is wrongly detected. This situation implies that at least one receive MSG in this SB has a higher power than the receive OSG, according to the detection criterion in (15). Notably, (12) constraints the power of OSGs α^{o} to exceed the maximum power of an MSG. Therefore, the location of OSG is most likely misjudged as the position of an MSG with the highest transmit power among all $F-1$ MSGs in this SB, with a probability of

$$P^{\mathrm{o}} \approx \sum_{r=1}^{\Lambda^{\mathrm{m}}} Q\left(\frac{\sqrt{\beta}(\alpha^{\mathrm{o}} - \mathcal{A}^{\mathrm{m}}(r))}{\sqrt{2\sigma^2(\mathcal{A}^{\mathrm{m}}(r) + \alpha^{\mathrm{o}})}}\right) P(\mathcal{A}^{\mathrm{m}}(r)), \quad (20)$$

where

$$P(\mathcal{A}^{\mathrm{m}}(r)) = \begin{cases} 1 - \left(\frac{\Lambda^{\mathrm{m}}-1}{\Lambda^{\mathrm{m}}}\right)^{F-1}, & r = 1 \\ 1 - \sum_{r'=1}^{r-1} P(\mathcal{A}^{\mathrm{m}}(r')) - \left(\frac{\Lambda^{\mathrm{m}}-r}{\Lambda^{\mathrm{m}}}\right)^{F-1}, & 2 \le r \le \Lambda^{\mathrm{m}}. \end{cases} \quad (21)$$

Here, we recall that $\mathcal{A}^{\mathrm{m}}$ is the set of all possible transmit powers for an MSG, with cardinality Λ^{m}. The elements in $\mathcal{A}^{\mathrm{m}}$ satisfy $\mathcal{A}^{\mathrm{m}}(1) \ge \mathcal{A}^{\mathrm{m}}(2) \ge \cdots \ge \mathcal{A}^{\mathrm{m}}(\Lambda^{\mathrm{m}})$. $P(\mathcal{A}^{\mathrm{m}}(r))$ represents the probability that the maximum transmit power of $F-1$ MSGs is $\mathcal{A}^{\mathrm{m}}(r)$, where $r \in \{1,2,\ldots,\Lambda^{\mathrm{m}}\}$. The derivation for (20) and (21) is provided in Appendix A.

In other words, an l^{o}-dimensional index bit stream for an SB may be detected as another l^{o}-dimensional bit stream with a probability of P^{o}, where the number of distinct error patterns is $F-1$. Among these $F-1$ error patterns, there are $C(l^{\mathrm{o}}, e^{\mathrm{o}})$ different patterns that result in e^{o} erroneous bits in the index bit stream, with $1 \le e^{\mathrm{o}} \le l^{\mathrm{o}}$. Accordingly, the average number of erroneous index bits for an SB is

$$\tilde{l}^{\mathrm{o}} = P^{\mathrm{o}} \sum_{e^{\mathrm{o}}=1}^{l^{\mathrm{o}}} C(l^{\mathrm{o}}, e^{\mathrm{o}}) e^{\mathrm{o}}. \quad (22)$$

2) Average Number of Erroneous Modulation Bits: According to the proposed decoupled detector in (15) and (16), it is observed that the detected location of OSG, i.e., $\hat{I}_g, g \in \{1,2,\ldots,G\}$, may affect the result of modulation signal detection. Therefore, for an SB, the average number of erroneous modulation bits $\tilde{l}^{\mathrm{m}}$ is related to two distinct terms: i) the average number of erroneous modulation bits when the location of OSG is correctly recovered; ii) the average number of erroneous modulation bits when the location of OSG is wrongly recovered.

Specifically, when the OSG is correctly identified, the detection for each transmit MSG is derived from its corresponding receive MSG. This leads to the following expression for the average number of erroneous bits in each MSG:

$$e^{\mathrm{m}} = \frac{1}{\Lambda^{\mathrm{m}}} \sum_{\mathbf{s}_1 \in \mathcal{S}^{\mathrm{m}}} \sum_{\substack{\mathbf{s}_2 \in \mathcal{S}^{\mathrm{m}} \\ \mathbf{s}_2 \ne \mathbf{s}_1}} P(\mathbf{s}_1 \to \mathbf{s}_2) H(\mathbf{s}_1 \to \mathbf{s}_2). \quad (23)$$

In (23), $\mathbf{s}_1, \mathbf{s}_2 \in \mathcal{S}^{\mathrm{m}}$ are two distinct combinations of MDS-IQM symbols for an MSG. Recall that $\mathcal{S}^{\mathrm{m}}$ is the set of all valid combinations of MDS-IQM symbols for an MSG, with cardinality Λ^{m}. $H(\mathbf{s}_1 \to \mathbf{s}_2)$ is the Hamming distance between the bit streams of $\mathbf{s}_1$ and $\mathbf{s}_2$. $P(\mathbf{s}_1 \to \mathbf{s}_2)$ is the PEP of detecting $\mathbf{s}_1$ as $\mathbf{s}_2$. Using the ML detection in (16), this PEP is approximated by [29]:

$$P(\mathbf{s}_1 \to \mathbf{s}_2) \approx Q\left(\sqrt{\frac{\beta\alpha^{\mathrm{m}}\|\mathbf{s}_1 - \mathbf{s}_2\|_F^2}{2\sigma^2}}\right). \quad (24)$$

Since each SB comprises $F-1$ MSGs, the average number of erroneous modulation bits when the OSG is correctly identified, denoted by $\tilde{l}_1^{\mathrm{m}}$, is given by

$$\tilde{l}_1^{\mathrm{m}} = (F-1)e^{\mathrm{m}}. \tag{25}$$

When the location of OSG is wrongly detected, it means that only partial MSGs can be recovered based on the corresponding receive MSGs. More specifically, let us assume that the OSG with index f_1 is wrongly recovered as f_2, with $f_1 \neq f_2$, $f_1, f_2 \in \{1, 2, \ldots, F\}$. Then, based (15) and (16), it is known that the $F-1$ transmit MSGs with indexes $\{1, \ldots, f_1-1, f_1+1, \ldots, F\}$ are estimated from the $F-1$ receive SGs indexed by $\{1, \ldots, f_2-1, f_2+1, \ldots, F\}$. By comparing these two index sets, it is observed that only the MSGs from the first to the $\min(f_1-1, f_2-1)$-th, as well as from the $\max(f_1+1, f_2+1)$-th to the last, are estimated based on their corresponding receive MSGs. For these $F-1-|f_1-f_2|$ MSGs, the average number of erroneous bits is given by $(F-1-|f_1-f_2|)e^{\mathrm{m}}$. For the remaining $|f_1-f_2|$ MSGs, i.e., the MSGs indexed from the $\min(f_1, f_2)$-th to the $\max(f_1, f_2)$-th, their modulation signals are detected without the knowledge of the corresponding receive signals. Hence, the average number of erroneous bits for these $|f_1-f_2|$ MSGs is $|f_1-f_2|l^{\mathrm{m}}/2$, recalling that l^{m} is the number of information bits conveyed by an MSG. Based on the above analysis, the average number of erroneous modulation bits when the OSG is wrongly identified, denoted by $\tilde{l}_2^{\mathrm{m}}$, is expressed as

$$\tilde{l}_2^{\mathrm{m}} = \frac{1}{F}\sum_{f_1=1}^{F}\sum_{\substack{f_2=1\\ f_2\neq f_1}}^{F}\Big((F-1-|f_1-f_2|)e^{\mathrm{m}} + |f_1-f_2|\frac{l^{\mathrm{m}}}{2}\Big). \tag{26}$$

At last, considering that the probability of misdetecting the location of OSG is P^{o} in (20), the overall average number of erroneous modulation bits, i.e., $\tilde{l}^{\mathrm{m}}$, is determined by a weighted sum of $\tilde{l}_1^{\mathrm{m}}$ and $\tilde{l}_2^{\mathrm{m}}$:

$$\tilde{l}^{\mathrm{m}} = (1-P^{\mathrm{o}})\tilde{l}_1^{\mathrm{m}} + P^{\mathrm{o}}\tilde{l}_2^{\mathrm{m}}. \tag{27}$$

By substituting the expression of $\tilde{l}^{\mathrm{o}}$ in (22) and the expression of $\tilde{l}^{\mathrm{m}}$ in (27) into (19), the BER of the proposed A-MDS-OFDM-IM waveform is finally given by

$$\begin{aligned}\mathrm{BER} = \frac{1}{l}\Bigg(&P^{\mathrm{o}}\sum_{e^{\mathrm{o}}=1}^{l^{\mathrm{o}}} C(l^{\mathrm{o}}, e^{\mathrm{o}})e^{\mathrm{o}} + (1-P^{\mathrm{o}})(F-1)e^{\mathrm{m}} + \cdots \\ &\frac{P^{\mathrm{o}}}{F}\sum_{f_1=1}^{F}\sum_{\substack{f_2=1\\ f_2\neq f_1}}^{F}\Big((F-1-|f_1-f_2|)e^{\mathrm{m}} + |f_1-f_2|\frac{l^{\mathrm{m}}}{2}\Big)\Bigg),\end{aligned} \tag{28}$$

with P^{o} and e^{m} given by (20) and (23), respectively.

B. PSL of the Proposed A-MDS-OFDM-IM

When γ_q is ignored for all $q \in \{1, 2, \ldots, Q\}$ in (17), it is demonstrated in [44] that the range estimation profile based on the sensing processes in Section II-C is equivalent to the periodic auto-correlation function (PACF) of the TD transmit signal stream $\mathbf{x}'$. Consequently, the sensing performance of the proposed A-MDS-OFDM-IM waveform is closely related to the PACF of $\mathbf{x}'$, defined as

$$r(i) = \sum_{i'=0}^{N-1} x'(i')(x'((i'-i) \bmod N))^* = r^*(-i),\ i = 0, 1, \ldots, N-1. \tag{29}$$

Specifically, waveforms with low PACF sidelobes are preferred to avoid the masking effect. Here, the masking effect refers to the phenomenon that the peak of a target with weak echo power is masked by the higher power sidelobes. The PACF sidelobe level of $\mathbf{x}'$ can be quantified by the PSL, defined as

$$\mathrm{PSL} = \max_{1\leq i\leq N-1} |r(i)|. \tag{30}$$

From (29), it is observed that the vector $[r(0), r(1), \ldots, r(N-1)]^T$ and the power spectrum of the FD transmit signal stream $\mathbf{x}$, denoted by $\mathbf{v} = [v(0), v(1), \ldots, v(N-1)]^T = [|x(0)|^2, |x(1)|^2, \ldots, |x(N-1)|^2]^T$, constitute a Fourier transform pair. Using this relationship, the PSL in (30) can be further expressed as

$$\mathrm{PSL} = \max_{1\leq i\leq N-1} |\mathbf{W}_i^H \mathbf{v}|, \tag{31}$$

where $\mathbf{W}_i \in \mathbb{C}^{N\times 1}$ is the i-th column of the discrete Fourier transform (DFT) matrix $\mathbf{W} \in \mathbb{C}^{N\times N}$.

C. PAPR of the Proposed A-MDS-OFDM-IM

To accurately estimate the PAPR of the continuous-time A-MDS-OFDM-IM waveform, it is essential to oversample the discrete TD transmit waveform $\mathbf{x}'$ by a factor no less than 4 [37]. Specifically, denoted by ϵ the oversampling factor, the normalized oversampled TD signal stream $\bar{\mathbf{x}} \in \mathbb{C}^{\epsilon N\times 1}$ is given by

$$\bar{\mathbf{x}} = \bar{\mathbf{W}}^H \mathbf{x}. \tag{32}$$

Here, $\bar{\mathbf{W}} \in \mathbb{C}^{N\times \epsilon N}$ is the DFT matrix with oversampling factor ϵ, with $W(n_1, n_2) = e^{-j2\pi n_1 n_2/\epsilon N}$ for $n_1 \in \{0, 1, \ldots, N-1\}$ and $n_2 \in \{0, 1, \ldots, \epsilon N-1\}$.

The PAPR of $\bar{\mathbf{x}}$ is defined as

$$\mathrm{PAPR} = \frac{\|\bar{\mathbf{x}}\|_\infty^2}{\|\bar{\mathbf{x}}\|_F^2/\epsilon N} = \frac{\|\bar{\mathbf{x}}\|_\infty^2}{\sum_{i=0}^{N-1} v(i)/N}, \tag{33}$$

where the second equation follows from the fact that $\|\bar{\mathbf{x}}\|_F^2 = \epsilon\|\mathbf{x}\|_F^2 = \epsilon\sum_{i=0}^{N-1} v(i)$, recalling that $\mathbf{v} = [v(0), v(1), \ldots, v(N-1)]^T$ is the power spectrum of $\mathbf{x}$.

IV. Adaptive Waveform Optimization for Low-Altitude ISAC

As described in Section II-A, the FD signals of OSGs are adaptively designed based on those of MSGs in each transmission. This section introduces the adaptive design criterion, aiming to jointly optimize the communication and sensing performance of the transmit waveform for low-altitude ISAC. Specifically, metrics including BER, PSL, and PAPR are considered in waveform optimization.

A. Problem Formulation

As indicated before, the goal of waveform optimization is to jointly optimize its BER in (28), PSL in (31), and PAPR in (33), which is constrained by the FD waveform structure in (1) to (3) and the power constraint on OSGs in (12). By plugging (12) into the expression of an FD SB in (3), this

optimization problem is formulated as:

$$\begin{aligned}&\min_{\mathbf{x},\alpha^{\mathrm{o}}} \{\text{BER in (28), PSL in (31), PAPR in (33)}\}\\ &\text{s.t. } C_1: \|\mathbf{x}_{g,I_g}\|_F^2=\alpha^{\mathrm{o}},\ g=1,2,\ldots,G\\ &\quad C_2: \mathbf{x}_{g,f}=\sqrt{\alpha^{\mathrm{m}}}\mathbf{s}^{\mathrm{m}}_{g,f},\ f=1,\ldots,I_g-1,I_g+1,\ldots,F\\ &\quad C_3: \mathcal{A}^{\mathrm{m}}(1)<\alpha^{\mathrm{o}}<\frac{N}{G}\\ &\quad C_4: \alpha^{\mathrm{m}}=\frac{N-G\alpha^{\mathrm{o}}}{G(F-1)},\end{aligned} \tag{34}$$

where the upper bound of α^{o} in C_3 ensures that $\alpha^{\mathrm{m}}>0$.

As shown in Section III, the BER of the proposed waveform depends solely on the value of α^{o}, and the PSL is determined by the power spectrum of $\mathbf{x}$, i.e., $\mathbf{v}=|\mathbf{x}|^2$. The PAPR is influenced by both the powers and phases of the FD transmit signals. Based on these observations, we decompose the optimization problem in (34) into three subproblems as

$$\begin{aligned}P_1: &\min_{\alpha^{\mathrm{o}}} \text{ BER in (28)}\\ &\text{s.t. } C_1, C_2, C_3, C_4,\end{aligned} \tag{35a}$$

$$\begin{aligned}P_2: &\min_{\mathbf{v}} \text{ PSL in (31)}\\ &\text{s.t. } C_1, C_2, C_4\\ &\quad \mathbf{v}=|\mathbf{x}|^2\\ &\quad \alpha^{\mathrm{o}}=\breve{\alpha}^{\mathrm{o}},\end{aligned} \tag{35b}$$

$$\begin{aligned}P_3: &\min_{\mathbf{x}} \text{ PAPR in (33)}\\ &\text{s.t. } C_2, C_4\\ &\quad |\mathbf{x}_{g,I_g}|^2=\breve{\mathbf{v}}_{g,I_g},\ g=1,2,\ldots,G.\end{aligned} \tag{35c}$$

In (35b), $\breve{\alpha}^{\mathrm{o}}$ denotes the optimal power of OSGs obtained by solving P_1. Similarly, $\breve{\mathbf{v}}$ in (35c) represents the optimal power spectrum of $\mathbf{x}$ from solving P_2, where the elements in $\breve{\mathbf{v}}$ are partitioned in the same manner as those in $\mathbf{x}$. As observed from (35a) to (35c), the primary objective of the optimization process is to minimize BER, followed by PSL minimization. The PAPR optimization is conducted under the constraint that neither the BER nor the PSL performance of the waveform is compromised.

B. BER Optimization by Solving P_1

In our proposed A-MDS-OFDM-IM transmitter, the BER optimization problem P_1 in (35a) is solved using a search-based method, where the optimal power of OSGs $\breve{\alpha}^{\mathrm{o}}$ is selected from a discrete set $\mathcal{A}^{\mathrm{o}}$. Specifically, we first define a step factor $\delta>0$, which represents the spacing between consecutive elements in $\mathcal{A}^{\mathrm{o}}$. Then, based on constraint C_3 in (34), the set $\mathcal{A}^{\mathrm{o}}$ is constructed as

$$\mathcal{A}^{\mathrm{o}}=\{\mathcal{A}^{\mathrm{m}}(1)+\delta, \mathcal{A}^{\mathrm{m}}(1)+2\delta,\ldots,\mathcal{A}^{\mathrm{m}}(1)+\Lambda^{\mathrm{o}}\delta\}, \tag{36}$$

where $\Lambda^{\mathrm{o}}=\lfloor (N/G-\mathcal{A}^{\mathrm{m}})/\delta \rfloor$ is the cardinality of $\mathcal{A}^{\mathrm{o}}$. Finally, $\breve{\alpha}^{\mathrm{o}}$ is selected as the element of $\mathcal{A}^{\mathrm{o}}$ that minimizes the BER expression in (28), i.e.,

$$\breve{\alpha}^{\mathrm{o}}=\underset{\alpha^{\mathrm{o}}\in\mathcal{A}^{\mathrm{o}}}{\operatorname{argmin}} \text{ (28)}. \tag{37}$$

The complexity of this search-based BER optimization algorithm is primarily determined by computing the theoretical BER in (28). Specifically, the complexity of computing (28) mainly arises from calculating e^{m} in (23) and the third term in (28). This leads to a complexity order of $O(n(\Lambda^{\mathrm{m}})^2+F^2)$, where Λ^{m} is the number of legitimate FD signal streams of an MSG and F is the number of SGs in an SB. Since the BER optimization involves calculating the theoretical BERs for a total of Λ^{o} different powers of OSGs, the overall complexity of the algorithm is $O(\Lambda^{\mathrm{o}}(n(\Lambda^{\mathrm{m}})^2+F^2))$. Notably, as shown in Section III-A, the theoretical BER of the proposed waveform remains invariant when the system parameters are fixed. Consequently, the BER optimization processes can be completed prior to transmission, without affecting the complexity during actual transmission.

C. PSL Optimization by Solving P_2

Based on the PSL in (31) and the optimal power of OSGs $\breve{\alpha}^{\mathrm{o}}$ obtained from (37), the PSL optimization problem P_2 in (35b) can be rewritten as

$$\begin{aligned}&\min_{\mathbf{v}} \max_{1\le i\le N-1} |\mathbf{W}_i^H\mathbf{v}|\\ &\text{s.t. } C_1^{\mathrm{s}}: \sum_{a=1}^{n} v_{g,I_g}(a)=\breve{\alpha}^{\mathrm{o}},\ g=1,2,\ldots,G\\ &\quad C_2^{\mathrm{s}}: \mathbf{v}_{g,f}=\frac{N-G\breve{\alpha}^{\mathrm{o}}}{G(F-1)}|\mathbf{s}^{\mathrm{m}}_{g,f}|^2; f=1,\ldots,I_g-1,I_g+1,\ldots,F\\ &\quad C_3^{\mathrm{s}}: v_{g,I_g}(a)\ge 0,\ a=1,2,\ldots,n.\end{aligned} \tag{38}$$

The constraints in (38) are convex, however, the maximization of the non-smooth objective function $|\mathbf{W}_i^H\mathbf{v}|$ is non-differentiable, making the problem in (38) non-convex.

To address this non-differentiability, we express the absolute values of the complex inner products in the objective function as functions of real variables, following the method in [48]. Specifically, we first define a real-valued matrix $\mathbf{W}_i'\in\mathbb{R}^{N\times 2}$, $i\in\{1,2,\ldots,N-1\}$, as

$$\mathbf{W}_i'=[\mathrm{Re}(\mathbf{W}_i),\mathrm{Im}(\mathbf{W}_i)],\ i=1,2,\ldots,N-1. \tag{39}$$

With this definition, we then reformulate the optimization problem in (38) as

$$\begin{aligned}&\min_{\mathbf{v}} \max_{1\le i\le N-1} \|(\mathbf{W}_i')^H\mathbf{v}\|_F^2\\ &\text{s.t. } C_1^{\mathrm{s}}, C_2^{\mathrm{s}}, C_3^{\mathrm{s}},\end{aligned} \tag{40}$$

whose objective function is equivalent to that of (38). (40) is a second-order cone programming (SOCP) problem, which is convex in nature and can be efficiently solved by convex optimization methods.

The complexity of solving (40) depends on the selected optimization algorithm. By utilizing advanced convex optimization tools like MATLAB's TFOCS, the solution process may exhibit linear complexity, i.e., $O(N)$.

D. PAPR Optimization by Solving P_3

Here, we first recall that the optimal power spectrum of $\mathbf{x}$ obtained from solving (40) is denoted by $\breve{\mathbf{v}}$. Since the power spectrum of $\mathbf{x}$ is fixed, it follows that the denominator of the PAPR expression in (33) is also fixed. Accordingly, the PAPR optimization problem P_3 in (35c) is simplified to

$$\begin{aligned}&\min_{\bar{\mathbf{x}},\mathbf{x}} \|\bar{\mathbf{x}}\|_\infty^2\\ &\text{s.t. } C_1^{\mathrm{p}}: \bar{\mathbf{x}}=\bar{\mathbf{W}}^H\mathbf{x}\\ &\quad C_2^{\mathrm{p}}: |\mathbf{x}_{g,I_g}|^2=\breve{\mathbf{v}}_{g,I_g},\ g=1,2,\ldots,G\\ &\quad C_3^{\mathrm{p}}: \mathbf{x}_{g,f}=\sqrt{\frac{N-G\breve{\alpha}^{\mathrm{o}}}{G(F-1)}}\mathbf{s}^{\mathrm{m}}_{g,f}, f=1,\ldots,I_g-1,I_g+1,\ldots,F.\end{aligned} \tag{41}$$

Due to the non-convex unimodular constraint C_2, the optimization problem in (41) is non-convex. In the following, we design an ADMM-based algorithm [49] to solve this non-convex problem.

Specifically, the augmented Lagrangian function of (41) is given by

$$L_\rho(\bar{\mathbf{x}}, \mathbf{x}, \mathbf{e}) = \|\bar{\mathbf{x}}\|_\infty^2 + \frac{\rho}{2}\|\bar{\mathbf{x}} - \bar{\mathbf{W}}^H\mathbf{x} + \mathbf{e}\|_F^2, \tag{42}$$

where $\rho > 0$ is the penalty factor, and $\mathbf{e} \in \mathbb{C}^{\epsilon N \times 1}$ is the scaled dual variable. Based on the concept of ADMM, we solve (42) by alternately updating the three variables $\{\bar{\mathbf{x}}, \mathbf{x}, \mathbf{e}\}$ as follows:

$$\bar{\mathbf{x}}^{(t)} = \underset{\bar{\mathbf{x}}}{\operatorname{argmin}}\ L_\rho(\bar{\mathbf{x}}, \mathbf{x}^{(t-1)}, \mathbf{e}^{(t-1)}) \tag{43a}$$

$$\mathbf{x}^{(t)} = \underset{\mathbf{x}}{\operatorname{argmin}}\ L_\rho(\bar{\mathbf{x}}^{(t)}, \mathbf{x}, \mathbf{e}^{(t-1)}) \tag{43b}$$

$$\mathbf{e}^{(t)} = \mathbf{e}^{(t-1)} + \rho(\bar{\mathbf{x}}^{(t)} - \bar{\mathbf{W}}^H\mathbf{x}^{(t)}), \tag{43c}$$

where the superscript t denotes the t-th iteration. The problems in (43a) and (43b) are solved below.

Step 1: Updating $\bar{\mathbf{x}}^{(t)}$ based on $\mathbf{x}^{(t-1)}$ and $\mathbf{e}^{(t-1)}$

According the augmented Lagrangian function in (42), the optimization problem in (43a) is formulated as

$$\min_{\bar{\mathbf{x}}}\ \|\bar{\mathbf{x}}\|_\infty^2 + \frac{\rho}{2}\|\bar{\mathbf{x}} - \bar{\mathbf{W}}^H\mathbf{x}^{(t-1)} + \mathbf{e}^{(t-1)}\|_F^2. \tag{44}$$

This problem is non-convex due to the non-convex nature of $\|\bar{\mathbf{x}}\|_\infty^2$. To address this, we introduce an auxiliary variable μ and transform the problem into the following equivalent form:

$$\begin{aligned} &\min_{\bar{\mathbf{x}},\mu}\ \mu^2 + \frac{\rho}{2}\|\bar{\mathbf{x}} - \bar{\mathbf{W}}^H\mathbf{x}^{(t-1)} + \mathbf{e}^{(t-1)}\|_F^2 \\ &\text{s. t. } \|\bar{\mathbf{x}}\|_\infty \le \mu. \end{aligned} \tag{45}$$

The resulting problem in (45) is a SOCP problem and can therefore be solved using classic convex optimization methods.

Step 2: Updating $\mathbf{x}^{(t)}$ based on $\bar{\mathbf{x}}^{(t)}$ and $\mathbf{e}^{(t-1)}$

Since the term $\|\bar{\mathbf{x}}\|_\infty^2$ in (42) is not a function of $\mathbf{x}$, the optimization problem in (43b) simplifies to

$$\begin{aligned} &\min_{\mathbf{x}}\ \|\bar{\mathbf{x}}^{(t)} - \bar{\mathbf{W}}^H\mathbf{x} + \mathbf{e}^{(t-1)}\|_F^2 \\ &\text{s. t. } C_2^{\mathrm{p}}, C_3^{\mathrm{p}}. \end{aligned} \tag{46}$$

This problem is a standard quadratic optimization problem, and its unconstrained solution is given by $\acute{\mathbf{x}}^{(t)} = \bar{\mathbf{W}}(\bar{\mathbf{x}}^{(t)} + \mathbf{e}^{(t-1)})$. By projecting this unconstrained solution onto constraints C_2 and C_3, we obtain the explicit solution for (46) as

$$x_{g,f}^{(t)}(a) = \begin{cases} \sqrt{v_{g,f}(a)}\frac{\acute{x}_{g,f}^{(t)}(a)}{|\acute{x}_{g,f}^{(t)}(a)|}, & f = I_g \\ \sqrt{\frac{N - G\breve{\alpha}^{\mathrm{o}}}{G(F-1)}}s_{g,f}^{\mathrm{m}}(a), & f \neq I_g, \end{cases} \tag{47}$$

for $g = 1, 2, \ldots, G$, $f = 1, 2, \ldots, F$, and $a = 1, 2, \ldots, n$. In (47), the elements of $\acute{\mathbf{x}}^{(t)}$ are divided in the same way as those of $\mathbf{x}$.

For clarity, **Algorithm 1** outlines the proposed ADMM-based approach for solving the PAPR optimization problem in (41), where $\bar{\mathbf{x}}^{(0)}$ and $\mathbf{x}^{(0)}$ are generated arbitrarily.

In each iteration, the complexity of this ADMM-based PAPR minimization algorithm is primarily determined by solving the SOCP problem in (45). As discussed in Section IV-C, the complexity of solving the SOCP problem can be linear when appropriate optimization tools are employed. Therefore, the overall complexity of the proposed PAPR minimization algorithm can be as low as $O(NT)$. Note that the execution time of an algorithm is deeply correlated with its computational complexity. Since each iteration of Algorithm 1 may operate with linear complexity, the cost per iteration in terms of execution time can also be expected to scale linearly with N.

Algorithm 1: ADMM-based PAPR optimization algorithm

Input: Penalty factor ρ, maximum iteration number T.
Initialization: $\bar{\mathbf{x}}^{(0)}$, $\mathbf{x}^{(0)}$, $\mathbf{e}^{(0)} = \mathbf{0}_N$, $t = 0$.
Output: Optimized FD transmit waveform $\mathbf{x}$.
Repeat
  Update $t = t + 1$.
  Update $\bar{\mathbf{x}}^{(t)}$ by solving (45).
  Update $\mathbf{x}^{(t)}$ using (47).
  Update $\mathbf{e}^{(t)}$ using (43c).
Until: $t = T$ or the value of objective function $\|\bar{\mathbf{x}}\|_\infty^2$ converged.

As shown in Section IV-B to Section IV-D, the BER optimization can be performed before transmission, while the optimizations of PSL and PAPR both have the potential to achieve linear complexity. Consequently, for each transmission, the proposed adaptive waveform optimization algorithm also holds the capacity to attain linear complexity.

V. Simulation Results

In this section, we conduct numerical simulations to evaluate the communication and sensing performance of the proposed A-MDS-OFDM-IM waveform. These results are compared to those of conventional OFDM-based waveforms with different modulation schemes, including conventional OFDM, OFDM-IM in [29], and MDS-IQM-OFDM in [33]. Moreover, the trade-off between the communication and sensing performance of A-MDS-OFDM-IM, as well as the convergence behavior of the proposed ADMM-based PAPR optimization algorithm are also discussed.

Specifically, BER and target detection probability are used to evaluate the communication and sensing performance of a waveform, respectively. In the figures of this section, "OFDM-IM (k_1, k_2, modulation type)" denotes the OFDM-IM waveform where k_2 subcarriers out of every k_1 subcarriers are activated and modulated by the selected modulation type. "MDS-IQM-OFDM (n, K, R, M)" stands for the MDS-IQM-OFDM waveform with n subcarriers in each SG, and the parameters of MDS-IQM are K, R, and M. Specifically, M is the PAM order, K and R denote the orders of I- and Q-branch modulation, respectively. A-MDS-OFDM-IM(G, $\breve{\alpha}^{\mathrm{o}}$) represents the A-MDS-OFDM-IM waveform where G SGs are selected as OSGs with a power of $\breve{\alpha}^{\mathrm{o}}$. The modulation parameters, i.e., n, K, R, and M, for the MSGs of A-MDS-OFDM-IM are identical to those of the comparing MDS-IQM-OFDM.

A. Simulation Setup and Performance Comparison

In this subsection, we compare the communication and sensing performance of different waveforms under different transmission rates. The solid-state power amplifier (SSPA) in

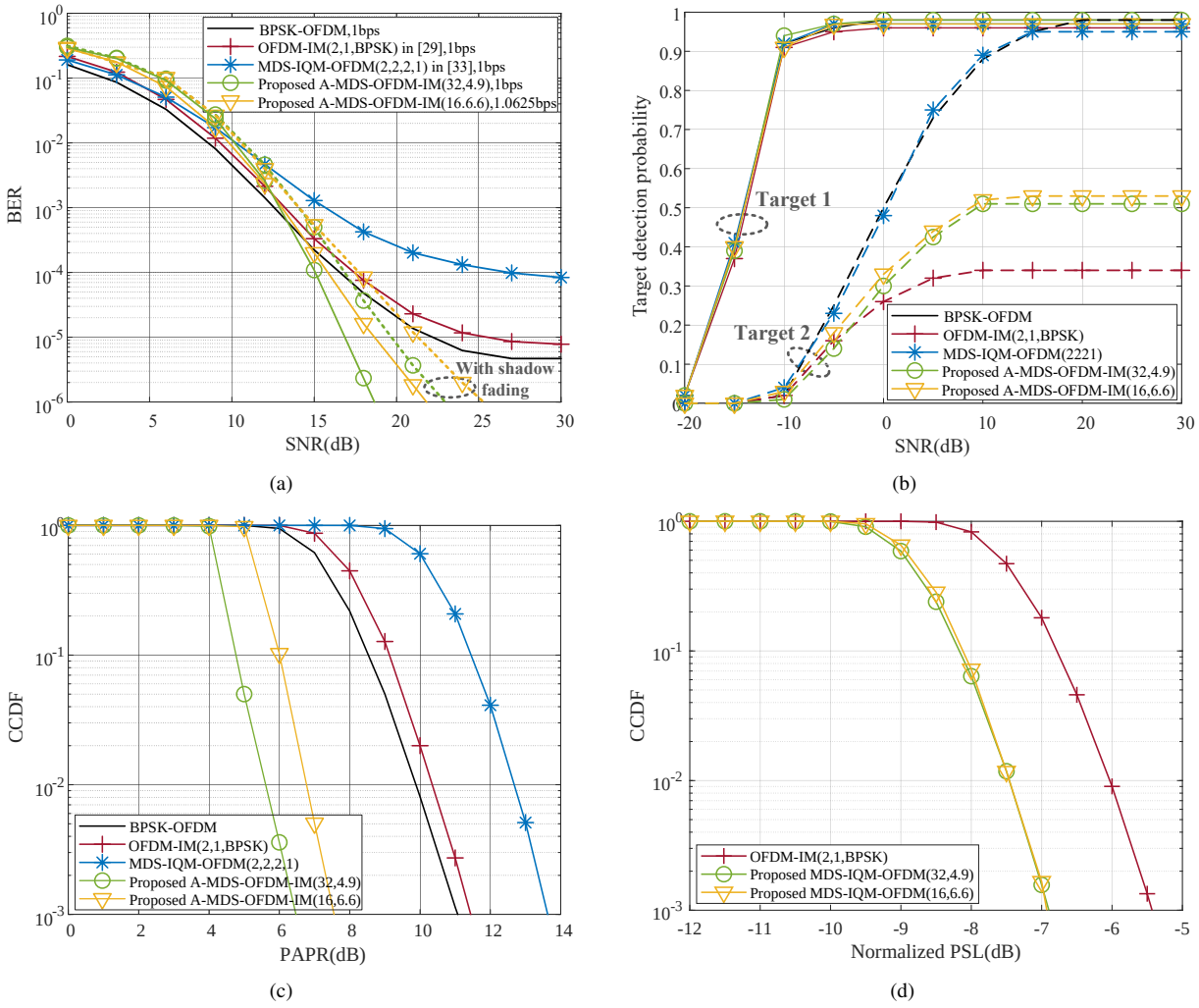

Fig. 2. Performance comparison under low modulation orders. (a) BER comparison with SSPA, IBO = 0 dB; (b) Target detection probability comparison; (c) PAPR comparison; (d) Normalized PSL comparison.

[38] is used, which converts the input amplitude A_{in} into

$$A_{\text{out}} = \frac{\omega A_{\text{in}}}{[1 + (A_{\text{in}}/A_{\text{sat}})^{2\eta}]^{1/2\eta}}. \tag{48}$$

In this SSPA model, ω denotes the amplifier gain, A_{sat} represents the saturation level of SSPA, and η is the smoothness parameter on the transition smoothness from the linear region to the saturated region. To reduce the signal nonlinear distortion at the SSPA, the input-back-off (IBO) operation [44], which reduces the powers of input signals, could be employed before amplification.

Based on the ISAC model in Fig. 1, our simulations consider a scenario where the UAV communicates with a user at 200 m, while simultaneously sensing two unauthorized targets at 100 and 300 m (namely Target 1 and Target 2), respectively. Since Target 2 is farther from the UAV, its peak may be masked by the sidelobes of Target 1, leading to Target 2 being missed. An OFDM symbol with 256 subcarriers is considered, with subcarrier spacing and carrier frequency being 240 kHz and 24 GHz, respectively. The radar cross-sections of both targets follow an exponential distribution with a rate parameter of 1 [50], [51]. For the SSPA model in (48), we set $\omega = 40$ dB, $A_{\text{sat}} = 1$, and $\eta = 2$. For the proposed A-MDS-OFDM-IM waveform, the step factor for BER optimization is $\delta = 0.1$, and the PAPR optimization parameters in **Algorithm 1** are penalty factor $\rho = 0.4$ and maximum iteration number $T = 1000$.

Fig. 2 compares the performance matrices including BER, target detection probabilities, PAPR, and normalized PSL of different waveforms under low modulation orders. Here, the signal-to-noise ratio (SNR) is defined as the ratio of the average receive power to the noise variance. The PAPR and PSL performance of each waveform is evaluated by the corresponding complementary cumulative distribution function (CCDF), which represents the probability that the PAPR or the normalized PSL exceeds a given threshold.

As observed from Fig. 2(a), MDS-IQM-OFDM fails to provide improved BER performance compared to BPSK-OFDM and OFDM-IM. The reason can be found in Fig. 2(c), which indicates that the PAPR of MDS-IQM-OFDM is higher than that of BPSK-OFDM and OFDM-IM. Therefore, the MDS-IQM-OFDM suffers the severest nonlinear distortion when passing through the SSPA, since IBO is not considered when modulation orders are low. The proposed A-MDS-OFDM-IM efficiently tackles this high-PAPR issue by adaptively optimizing the FD signals of OSGs, resulting in optimal BER performance at high SNRs. Note that a low PAPR also helps suppress the out-of-band emission (OOBE) of the waveform. Fig. 2(a) also provides the BERs of A-MDS-OFDM-IM waveforms under shadow fading, where the shadow fading is modeled as a Gaussian random variable with zero mean and 1 dB variance. From the results in Fig. 2(a), it is observed

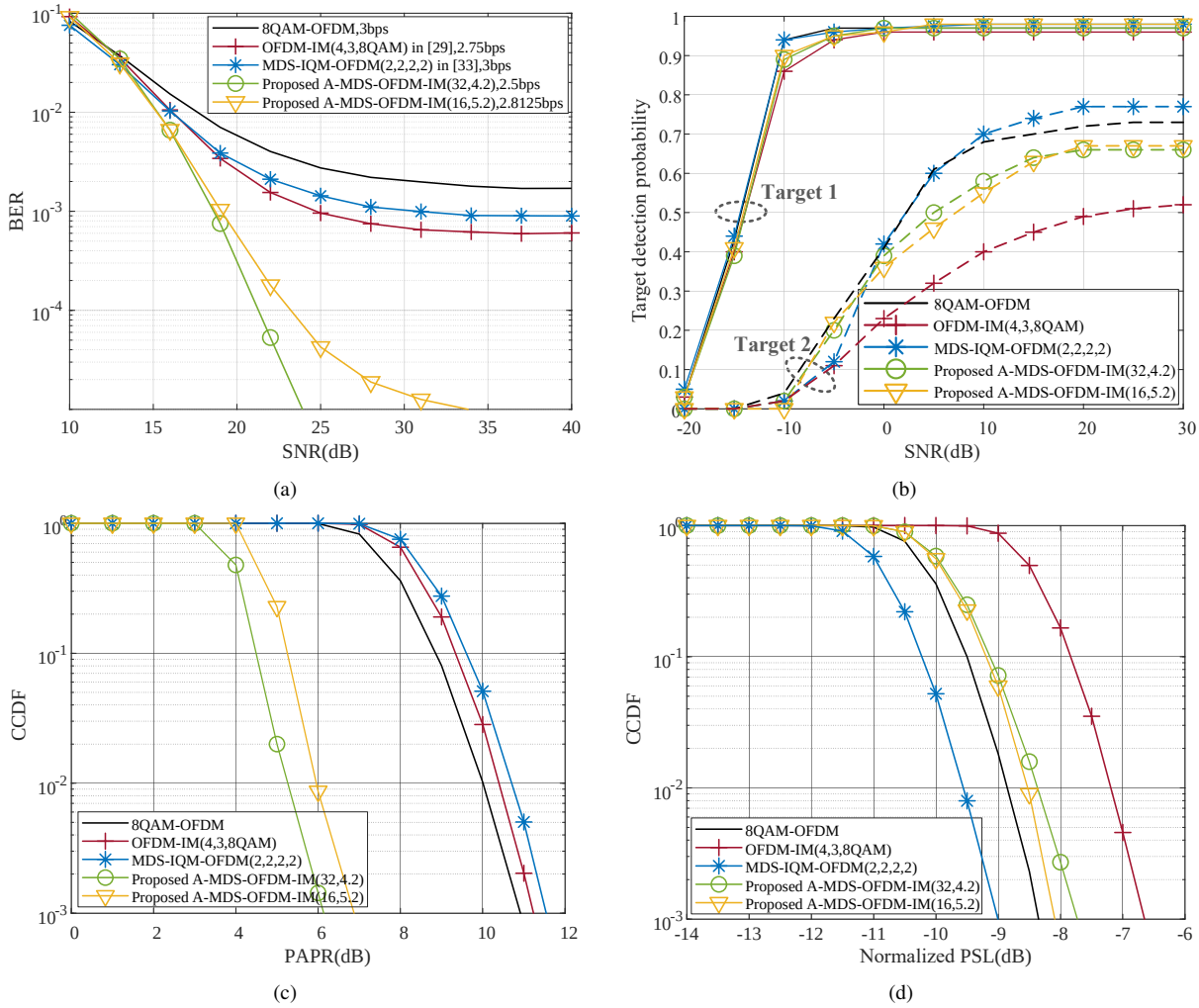

Fig. 3. Performance comparison under high modulation orders. (a) BER comparison with SSPA, IBO = 3 dB; (b) Target detection probability comparison; (c) PAPR comparison; (d) Normalized PSL comparison.

that A-MDS-OFDM-IM exhibits a degree of adaptability to the effect of shadow fading.

For the sensing performance, it is observed from Fig. 2(b) that when SNR exceeds -10 dB, all the four OFDM-based waveforms can detect Target 1 with a probability close to 1. However, only BPSK-OFDM and MDS-IQM-OFDM can identify Target 2 with a probability close to 1 in high SNR ranges. This is because, with the modulation configurations in Fig. 2, the FD signals of BPSK-OFDM and MDS-IQM-OFDM are unimodular, which leads to optimal PSL performance. The proposed A-MDS-OFDM-IM exhibits higher detection probability for Target 2 than OFDM-IM, since its PSL performance is better than that of OFDM-IM, as shown in Fig. 2(d). Note that compared with conventional MDS-IQM-OFDM, A-MDS-OFDM-IM(16,6.6) achieves a slightly increased SE, owing to the additional transmitted index bits.

By considering higher modulation orders, Fig. 3 presents the performance comparisons of different waveforms. In Fig. 3(a), the BERs of the two A-MDS-OFDM-IM waveforms can be reduced to 10^{-5} in high SNR regions when IBO is 3 dB, thanks to their low-PAPR characteristics shown in Fig. 3(c). However, the BERs of other waveforms are higher than 10^{-4} at all SNRs, since their PAPRs are about 5 dB higher than those of A-MDS-OFDM-IM waveforms. Although the BERs of these waveforms can be reduced by further increasing the value of IBO, this is at the cost of reduced amplifier efficiency. In addition, a higher IBO means lower transmission powers, which may also affect the communication and sensing performance. Moreover, the results in Figs. 2(c) and 3(c) indicate that increasing the number of OSGs is beneficial for reducing the PAPR and OOBE of A-MDS-OFDM-IM. Specifically, when CCDF is 10^{-3}, the PAPR of A-MDS-OFDM-IM with 32 OSGs is approximately 1 dB lower than that with 16 OSGs, despite a lower power of OSGs in the 32-OSG configuration.

As observed from Fig. 3(b), the target detection probabilities of A-MDS-OFDM-IM waveforms become closer to those of 8QAM-OFDM and MDS-IQM-OFDM under high modulation orders. This is because the PSLs of 8QAM-OFDM, MDS-IQM-OFDM, and A-MDS-OFDM-IM are close. That is to say, when modulation orders are high, the proposed A-MDS-OFDM-IM can simultaneously provide reliable communication and sensing with SSPA.

B. Trade-off Between the Communication and Sensing Performance of the Proposed A-MDS-OFDM-IM

As indicated in Section IV-A, in waveform optimization processes, the primary objective is the BER, followed by the PSL. That is to say, the optimized power of the OSGs $\breve{\alpha}^{\mathrm{o}}$ achieves the optimal communication performance, but its

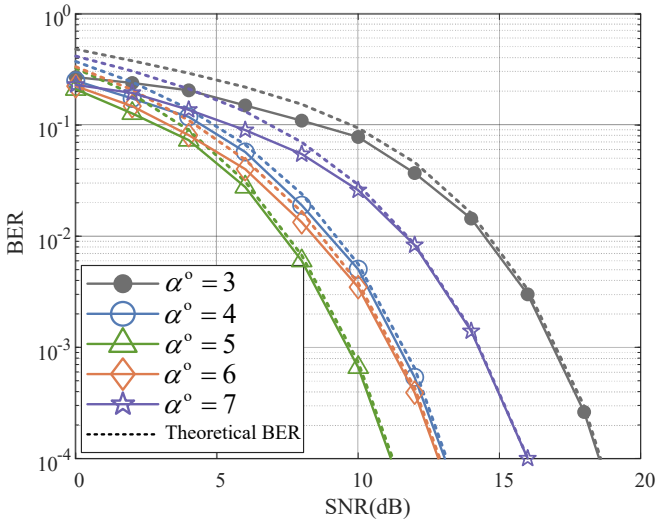

Fig. 4. BERs of the proposed A-MDS-OFDM-IM with different powers of OSGs α^{o}.

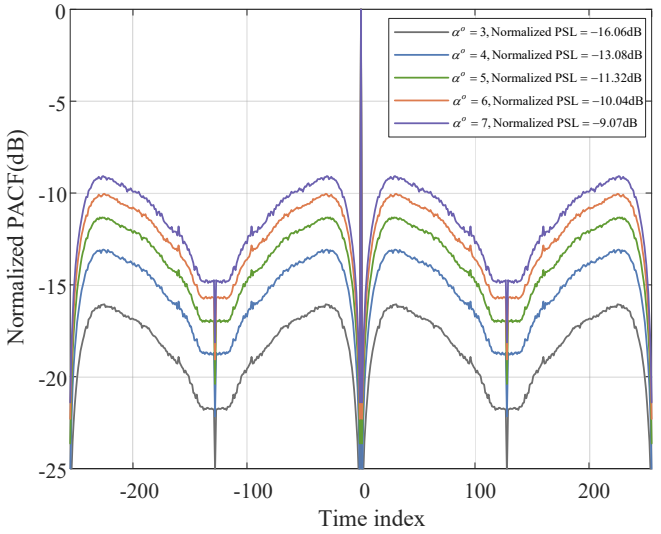

Fig. 5. Range profiles of the proposed A-MDS-OFDM-IM with different powers of OSGs α^{o}.

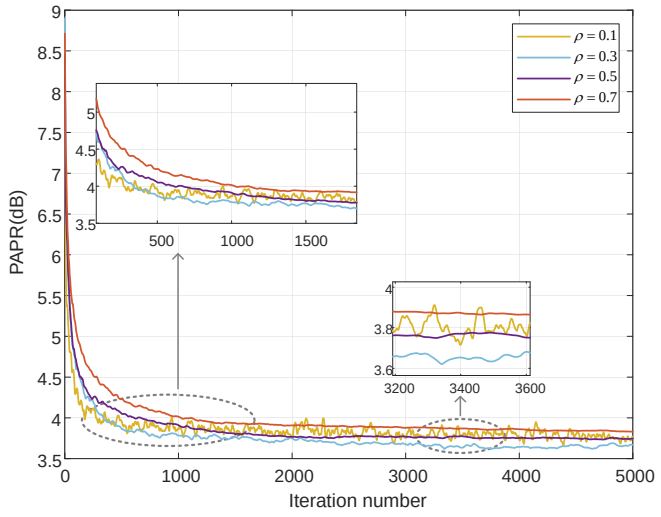

Fig. 6. Convergence behaviors of PAPR of A-MDS-OFDM-IM with different value of penalty factor ρ.

sensing performance may not be optimal. Considering this, simulations are conducted to show the impact of the value of α^{o} on both the theoretical BER in (28) and the range profile defined in (29). By considering the A-MDS-OFDM-IM with 1 bps transmission rate in Fig. 2, the BER and range profile results with different values of α^{o} are shown in Figs. 4 and 5. Note that as indicated in Section III-B, the range profile of a waveform is identical to its PACF. Moreover, to validate the theoretical BER in (28), the simulated BER results are also provided in Fig. 4.

As we can see, with an increase in the value of α^{o}, the BER performance initially improves and then decreases, while the sensing sidelobes keep increasing. For example, when $\alpha^{\text{o}} = 4$, the average normalized PSL of A-MDS-OFDM-IM is -13.08 dB, which is lower than the PSL of MDS-IQM-OFDM, since Fig. 2(d) indicates that the PSL of MDS-IQM-OFDM exceeds -13.08 dB with a probability of 1. Therefore, the value of α^{o} can be flexibly adjusted according to practical requirements. For instance, in scenarios with stringent sensing performance requirements, the power of OSGs can be appropriately reduced to achieve better sensing performance. Moreover, Fig. 4 also proves the correctness of the theoretical BER in (28). Specifically, with different values of α^{o}, the theoretical BERs are nearly identical to their corresponding simulated results in high SNRs.

C. Convergence Behavior of the Proposed ADMM-Based Algorithm

Finally, we conduct simulations to show the convergence behaviors of the proposed ADMM-based PAPR optimization algorithm with different values of the penalty factor ρ. The results are given in Fig. 6, where we also use the A-MDS-OFDM-IM waveform with 1 bps transmission rate. As shown in Fig. 6, for different values of ρ, the PAPR of the A-MDS-OFDM-IM waveform can all converge to a low value. Here, a smaller value of ρ leads to faster convergence. For instance, when $\rho = 0.1$, the PAPR converges after approximately 200 iterations, while when $\rho = 0.7$, it converges after around 1000 iterations. This is because a smaller penalty factor reduces the impact of constraints, thus enabling faster convergence. However, an excessively small penalty factor may lead to instability in the iteration results, as exemplified by the convergence curve for $\rho = 0.1$. Although a large value of the penalty factor can ensure the stability of the iteration process, it may result in a final convergence outcome that is less optimal compared to the result obtained with a smaller penalty factor. For example, the convergence curve for $\rho = 0.7$ is more stable than that for $\rho = 0.3$, but its achieved PAPR value is slightly increased.

VI. Conclusion

In this paper, we proposed an adaptive ISAC waveform for LAE applications, namely A-MDS-OFDM-IM, which jointly leverages the advantages of MDS code, IM, and OFDM. We analyzed the BER, PSL, and PAPR of the proposed UAV-assisted A-MDS-OFDM-IM system. Using these theoretical results, an adaptive design criterion was developed based on ADMM, which jointly optimized the system's BER, PSL, and PAPR. Numerical results demonstrated that A-MDS-OFDM-IM exhibits significantly reduced PAPR compared to conventional OFDM-based waveforms, making it outperform the benchmarks in terms of BER performance under a non-ideal HPA. Meanwhile, the proposed waveform also maintains

robust sensing performance with a relatively low PSL. The trade-off between the communication and sensing performance of A-MDS-OFDM-IM was further discussed, indicating that the proposed waveform can realize better sensing performance than benchmarks at the cost of slightly increased BER.

In the future, the extension of the proposed waveform to multi-user and multi-static scenarios will be further explored. Moreover, the applications of the proposed framework in some specialized LAE scenarios, such as the high-mobility environments modeled by doubly selective channels, will also be investigated.

APPENDIX A
DERIVATION FOR (20) AND (21)

To elaborate, let us focus on the g-th SB and assume that the I_g'-th MSG has the highest transmit power among all the $F-1$ MSGs in the g-th SB, with $g \in \{1,2,\ldots,G\}$ and $I_g' \in \{1,2,\ldots,F\}\backslash I_g$. Recall that I_g is the location of OSG in the g-th SB. With this assumption, P^{o} is identical to the pairwise error probability (PEP) $P(I_g \to I_g')$, which can be calculated by

$$P(I_g \to I_g') = \sum_{r=1}^{\Lambda^{\mathrm{m}}} P(I_g \to I_g' | \|\mathbf{x}_{g,I_g'}\|_F^2 = \mathcal{A}^{\mathrm{m}}(r)) P(\mathcal{A}^{\mathrm{m}}(r)), \tag{49}$$

where $P(I_g \to I_g' | \|\mathbf{x}_{g,I_g'}\|_F^2 = \mathcal{A}^{\mathrm{m}}(r))$ is the conditional PEP (CPEP) for misjudging I_g as I_g' when the transmit power of $\mathbf{x}_{g,I_g'}$ is $\mathcal{A}^{\mathrm{m}}(r)$.

To compute (49), we first analyze the CPEP $P(I_g \to I_g' | \|\mathbf{x}_{g,I_g'}\|_F^2 = \mathcal{A}^{\mathrm{m}}(r))$. According to the detection criterion in (15), this CPEP can be approximated by

$$\begin{aligned}
&P(I_g \to I_g' | \|\mathbf{x}_{g,I_g'}\|_F^2 = \mathcal{A}^{\mathrm{m}}(r)) \\
&\approx P(\|\mathbf{y}_{g,I_g}^{\mathrm{c}}\|_F^2 < \|\mathbf{y}_{g,I_g'}^{\mathrm{c}}\|_F^2 | \|\mathbf{x}_{g,I_g'}\|_F^2 = \mathcal{A}^{\mathrm{m}}(r)) \\
&\overset{\text{(a)}}{=} P(\beta(\alpha^{\mathrm{o}} - \mathcal{A}^{\mathrm{m}}(r)) + 2\,\mathrm{Re}(\sqrt{\beta}(\mathbf{s}_g^{\mathrm{o}})^H \mathbf{z}_{g,I_g}) - \cdots \\
&\qquad 2\,\mathrm{Re}(\sqrt{\beta\alpha^{\mathrm{m}}}(\mathbf{s}_{g,I_g'}^{\mathrm{m}})^H \mathbf{z}_{g,I_g'}) + \|\mathbf{z}_{g,I_g}\|_F^2 - \|\mathbf{z}_{g,I_g'}\|_F^2 < 0) \\
&\overset{\text{(b)}}{=} P(\zeta < 0),
\end{aligned} \tag{50}$$

where $\mathbf{z}_{g,f} \in \mathbb{C}^{n\times 1}$ denotes the AWGN for the f-th SG in the g-th SB, $g \in \{1,2,\ldots,G\}$, $f \in \{1,2,\ldots,F\}$. In (50), (a) is obtained by using the expression of $\mathbf{y}^{\mathrm{c}}$ in (14), the expression of $\mathbf{x}_{g,f}$ ($f \neq I_g$) in (3), as well as the equations $\|\mathbf{s}_g^{\mathrm{o}}\|_F^2 = \alpha^{\mathrm{o}}$ and $\|\sqrt{\alpha^{\mathrm{m}}}\mathbf{s}_{g,I_g'}\|_F^2 = \mathcal{A}^{\mathrm{m}}(r)$. The term ζ in (b) is called the decision variable. Since the elements of $\mathbf{z}_{g,I_g}$ and $\mathbf{z}_{g,I_g'}$ are independent and identically distributed Gaussian variables obeying $\mathcal{CN}(0,\sigma^2)$, it follows that ζ is a Gaussian random variable obeying $\mathcal{CN}(\beta(\alpha^{\mathrm{o}} - \mathcal{A}^{\mathrm{m}}(r)), 2\beta\sigma^2(\mathcal{A}^{\mathrm{m}}(r) + \alpha^{\mathrm{o}}))$. As a result, the CPEP in (50) is given by

$$P(I_g \to I_g' | \|\mathbf{x}_{g,I_g'}\|_F^2 = \mathcal{A}^{\mathrm{m}}(r)) \approx Q\left(\frac{\sqrt{\beta}(\alpha^{\mathrm{o}} - \mathcal{A}^{\mathrm{m}}(r))}{\sqrt{2\sigma^2(\mathcal{A}^{\mathrm{m}}(r) + \alpha^{\mathrm{o}})}}\right). \tag{51}$$

By substituting (51) into (49), we obtain the expression for the P^{o} in (20).

Subsequently, we proceed to calculate $P(\mathcal{A}^{\mathrm{m}}(r))$, the probability that the maximum transmit power of $F-1$ MSGs is $\mathcal{A}^{\mathrm{m}}(r)$. Given that the elements of $\mathcal{A}^{\mathrm{m}}$ are ordered as $\mathcal{A}^{\mathrm{m}}(1) \geq \mathcal{A}^{\mathrm{m}}(2) \geq \cdots \geq \mathcal{A}^{\mathrm{m}}(\Lambda^{\mathrm{m}})$, we first compute $P(\mathcal{A}^{\mathrm{m}}(1))$ by

$$\begin{aligned}
P(\mathcal{A}^{\mathrm{m}}(1)) &= 1 - \prod_{\substack{f=1 \\ f\neq I_g}}^{F} P(\|\mathbf{x}_{g,f}\|_F^2 < \mathcal{A}^{\mathrm{m}}(1)) \\
&\overset{\text{(a)}}{=} 1 - \prod_{\substack{f=1 \\ f\neq I_g}}^{F} \frac{C(\Lambda^{\mathrm{m}}-1,1)}{C(\Lambda^{\mathrm{m}},1)} = 1 - \Big(\frac{\Lambda^{\mathrm{m}}-1}{\Lambda^{\mathrm{m}}}\Big)^{F-1}.
\end{aligned} \tag{52}$$

In (52), the term $\prod_{f=1,f\neq I_g}^{F} P(\|\mathbf{x}_{g,f}\|_F^2 < \mathcal{A}^{\mathrm{m}}(1))$ calculates the probability that the transmit powers of all $F-1$ MSGs remain below $\mathcal{A}^{\mathrm{m}}(1)$, based on the fact that the $F-1$ MSGs are independent of each other. (a) of (52) holds because the power of each MSG is selected from $\mathcal{A}^{\mathrm{m}}$ with an equal probability $1/\Lambda^{\mathrm{m}}$. Using the expression of $P(\mathcal{A}^{\mathrm{m}}(1))$ in (52), we can then calculate $P(\mathcal{A}^{\mathrm{m}}(2))$ through

$$\begin{aligned}
P(\mathcal{A}^{\mathrm{m}}(2)) &= 1 - P(\mathcal{A}^{\mathrm{m}}(1)) - \prod_{\substack{f=1 \\ f\neq I_g}}^{F} P(\|\mathbf{x}_{g,f}\|_F^2 < \mathcal{A}^{\mathrm{m}}(2)) \\
&= 1 - P(\mathcal{A}^{\mathrm{m}}(1)) - \Big(\frac{\Lambda^{\mathrm{m}}-2}{\Lambda^{\mathrm{m}}}\Big)^{F-1}.
\end{aligned} \tag{53}$$

This derivation can be applied iteratively, leading to the general expression for $P(\mathcal{A}^{\mathrm{m}}(r))$ in (21).

REFERENCES

[1] Y. Jiang, X. Li, G. Zhu, H. Li, J. Deng, K. Han, C. Shen, Q. Shi, and R. Zhang, "6G non-terrestrial networks enabled low-altitude economy: Opportunities and challenges," *arXiv e-prints*, May 2024.

[2] "IEEE approved draft standard for a framework for structuring low altitude airspace for unmanned aerial vehicle (UAV) operations," *IEEE P1939.1/D6.0, October 2020*, pp.1-92, Sept. 2021.

[3] C. Huang, S. Fang, H. Wu, Y. Wang, and Y. Yang, "Low-altitude intelligent transportation: System architecture, infrastructure, and key technologies," *J. Ind. Inf. Integr.*, vol. 42, pp. 100694, Nov. 2024.

[4] Y. Yang, Y. Chen, J. Wang, G. Sun, and D. Niyato, "Embodied AI-empowered low altitude economy: Integrated sensing, communications, computation, and control (ISC3)," *arXiv e-prints*, Dec. 2024.

[5] H. Huang, J. Su, and F. Wang, "The potential of low-altitude airspace: The future of urban air transportation," *IEEE Trans. Intell. Veh.*, vol. 9, no. 8, pp. 5250-5254, Aug. 2024.

[6] Y. Chen, D. Yang, L. Xiao, F. Wu, and Y. Xu, "Optimal trajectory design for unmanned aerial vehicle cargo pickup and delivery system based on radio map," *IEEE Trans. Veh. Technol.*, vol. 73, no. 8, pp. 11706-11718, Aug. 2024.

[7] M. Ponti, A. Chaves, F. Jorge, G. Costa, A. Colturato, and K. Branco, "Precision agriculture: Using low-cost systems to acquire low-altitude images," *IEEE Comput. Graph. Appl.*, vol. 36, no. 4, pp. 14-20, Aug. 2016.

[8] T. Ernest, A. Madhukumar, R. Sirigina, and A. Krishnab, "Addressing spectrum efficiency through hybrid-duplex UAV communications: Challenges and opportunities," *Veh. Commun.*, vol. 24, pp. 100235, Aug. 2020.

[9] Z. Li, Z. Gao, K. Wang, Y. Mei, C. Zhu, L. Chen, X. Wu, and D. Niyato, "Unauthorized UAV countermeasure for low-altitude economy: Joint communications and jamming based on MIMO cellular systems," *IEEE Internet Things J.*, vol. 12, no. 6, pp. 6659-6672, Mar. 2025.

[10] Z. Kuang, W. Liu, C. Wang, Z. Jin, J. Ren, X. Zhang, and Y. Shen, "Movable-antenna array empowered ISAC systems for low-altitude economy," *IEEE ICCC Workshops*, Hangzhou, China, 2024, pp. 776-781.

[11] G. Cheng, X. Song, Z. Lyu, and J. Xu, "Networked ISAC for low-altitude economy: Transmit beamforming and UAV trajectory design," *IEEE ICCC Workshops*, Hangzhou, China, 2024, pp. 78-83.

[12] Z. Ye, Z. Zhou, P. Fan, Z. Liu, X. Lei, and X. Tang, "Low ambiguity zone: Theoretical bounds and doppler-resilient sequence design in integrated sensing and communication systems," *IEEE J. Sel. Areas Commun.*, vol. 40, no. 6, pp. 1809-1822, Jun. 2022.

[13] F. Liu, Y. Cui, C. Masouros, J. Xu, T. Han, Y. Eldar, and S. Buzzi, "Integrated sensing and communications: Toward dual-functional wireless networks for 6G and beyond," *IEEE J. Sel. Areas Commun.*, vol. 40, no. 6, pp. 1728-1767, Jun. 2022.

[14] F. Liu, C. Masouros, A. Petropulu, H. Griffiths, and L. Hanzo, "Joint radar and communication design: Applications, state-of-the-art, and the road ahead," *IEEE Trans. Commun.*, vol. 68, no. 6, pp. 3834-3862, Jun. 2020.

[15] X. Ye, Y. Mao, X. Yu, S. Sun, L. Fu, and J. Xu, "Integrated sensing and communications for low-altitude economy: A deep reinforcement learning approach," *arXiv e-prints*, Dec. 2024.

[16] C. Sturm and W. Wiesbeck, "Waveform design and signal processing aspects for fusion of wireless communications and radar sensing," *Proc. IEEE*, vol. 99, no. 7, pp. 1236-1259, Jul. 2011.

[17] A. Liu, Z. Huang, M. Li, Y. Wan, W. Li, T. X. Han, C. Liu, R. Du, D. Tan, J. Lu, Y. Shen, F. Colone, and K. Chetty, "A survey on fundamental limits of integrated sensing and communication," *IEEE Commun. Surv. Tutor.*, vol. 24, no. 2, pp. 994-1034, Feb. 2022.

[18] W. Zhou, R. Zhang, G. Chen, and W. Wu, "Integrated sensing and communication waveform design: A survey," *IEEE Open J. Commun. Soc.*, vol. 3, pp. 1930-1949, Oct. 2022.

[19] S. Liyanaarachchi, T. Riihonen, C. Barneto, and M. Valkama, "Optimized waveforms for 5G-6G communication with sensing: Theory, simulations and experiments," *IEEE Trans. Wireless Commun.*, vol. 20, no. 12, pp. 8301-8315, Dec. 2021.

[20] B. Zheng and F. Liu, "Random signal design for joint communication and SAR imaging towards low-altitude economy," *IEEE Wireless Commun. Lett.*, vol. 13, no. 10, pp. 2662-2666, Oct. 2024.

[21] Z. Xiao, R. Liu, M. Li, Q. Liu, and A. Swindlehurst, "A novel joint angle-range-velocity estimation method for MIMO-OFDM ISAC systems," *IEEE Trans. Signal Process.*, vol. 72, pp. 3805-3818, Aug. 2024.

[22] Z. Zhang, H. Ren, C. Pan, S. Hong, D. Wang, J. Wang, and X. You, "Target localization in cooperative ISAC systems: A scheme based on 5G NR OFDM signals," *IEEE Trans. Commun.*, vol. 73, no. 5, pp. 3562-3578, May 2025.

[23] F. Zhang, T. Mao, R. Liu, Z. Han, S. Chen, and Z. Wang, "Cross-domain dual-Functional OFDM waveform design for accurate sensing/positioning," *IEEE J. Sel. Areas Commun.*, vol. 42, no. 9, pp. 2259-2274, Sept. 2024.

[24] F. Liu, Y. Zhang, Y. Xiong, S. Li, W. Yuan, F. Gao, S. Jin, and G. Caire, "OFDM achieves the lowest ranging sidelobe under random ISAC signaling," *arXiv e-prints*, Oct. 2024.

[25] Y. Chen, G. Liao, Y. Liu, H. Li, and X. Liu, "Joint subcarrier and power allocation for integrated OFDM waveform in RadCom systems," *IEEE Commun. Lett.*, vol. 27, no. 1, pp. 253-257, Jan. 2023.

[26] Z. Du, F. Liu, Y. Xiong, T. Han, Y. Eldar, and S. Jin, "Reshaping the ISAC tradeoff under OFDM signaling: A probabilistic constellation shaping approach," *IEEE Trans. Signal Process.*, vol. 72, pp. 4782-4797, Sept. 2024.

[27] S. Li, F. Wang, Y. Zhang, R. Li, S. Shi, and Y. Li, "OFDM-MIMO radar assisted dual-function radar communication system using index modulation," *Digit. Signal Process.*, vol. 145, pp. 104302, Feb. 2024.

[28] G. Huang, Y. Ding, S. Ouyang, and V. Fusco, "Index modulation for OFDM RadCom systems," *J. Eng.*, vol. 2, pp. 61-72, Jan. 2021.

[29] E. Basar, U. Aygolu, E. Panayirci, and H. Poor, "Orthogonal frequency division multiplexing with index modulation," *IEEE Trans. Signal Process.*, vol. 61, no. 22, pp. 5536-5549, Nov. 2013.

[30] Q. Li, M. Wen, B. Clerckx, S. Mumtaz, A. Al-Dulaimi, and R. Hu, "Subcarrier index modulation for future wireless networks: Principles, applications, and challenges," *IEEE Wireless Commun.*, vol. 27, no. 3, pp. 118-125, Jun. 2020.

[31] H. Hawkins, C. Xu, L. Yang, and L. Hanzo, "IM-OFDM ISAC outperforms OFDM ISAC by combining multiple sensing observations," *IEEE Open J. Veh. Technol.*, vol. 5, pp. 312-329, Feb. 2024.

[32] Z. Yang, S. Gao, X. Cheng, and L. Yang, "Superposed IM-OFDM (S-IM-OFDM): An enhanced OFDM for integrated sensing and communications," *IEEE Trans. Veh. Technol.*, vol. 73, no. 10, pp. 15832-15836, Oct. 2024.

[33] F. Yarkin and J. Coon, "Modulation based on a simple MDS code: Achieving better error performance than index modulation and related schemes," *IEEE Trans. Commun.*, vol. 70, no. 1, pp. 118-131, Jan. 2022.

[34] F. Yarkin and J. Coon, "Comparing minimum codeword distances and error performance for index modulation and maximum distance separable coded modulation," *EuCNC/6G Summit*, Grenoble, France, 2022, pp.106-111.

[35] Y. Huang, P. Yang, V. Mordachev, and Gang Wu, "A generalized maximum distance separable coded framework design for vehicular RadCom," *IEEE ICCT*, Chengdu, China, 2024, pp. 669-674.

[36] Y. Huang, P. Yang, S. Zammit, N. Yang, G. Wu, and V. Mordachev, "A dual-function OFDM waveform design for future multicarrier communication," *IEEE Commun. Lett.*, vol. 28, no. 7, pp. 1624-1628, Jul. 2024.

[37] Y. Rahmatallah and S. Mohan, "Peak-to-average power ratio reduction in OFDM systems: A survey and taxonomy," *IEEE Commun. Surv. Tutorials*, vol. 15, no. 4, pp. 1567-1592, Mar. 2013.

[38] C. Rapp, "Effects of HPA-nonlinearity on a 4-DPSK/OFDM signal for a digital sound broadcasting system," *Proc. of the Second European Conference on Satellite Communications*, Liege, Belgium, 1991, pp. 179-184.

[39] Z. Wei, H. Qu, Y. Wang, X. Yuan, H. Wu, Y. Du, K. Han, N. Zhang, and Z. Feng, "Integrated sensing and communication signals toward 5G-A and 6G: A survey," *IEEE Internet Things J.*, vol. 10, no. 13, pp. 11068-11092, Jul. 2023.

[40] J. Zhang, M. Rahman, K. Wu, X. Huang, Y. Guo, S. Chen, and J. Yuan, "Enabling joint communication and radar sensing in mobile networks-A survey," *IEEE Commun. Surv. Tutor.*, vol. 24, no. 1, pp. 306-345, Oct. 2021.

[41] A. Bourdoux, M. Bauduin, and C. Desset, "IQ imbalance robust and low PAPR OFDM radar waveform," *IEEE RadarConf*, Boston, USA, 2019, pp. 1-6.

[42] Y. Liu, F. Cheng, J. Yi, Y. Rao, and X. Wan, "PAPR and sidelobe reduction using tone reservation in OFDM RadCom systems," *IEEE Sens. J.*, vol. 24, no. 16, pp. 26645-26658, Aug. 2024.

[43] R. Yao, Z. Wei, L. Su, L. Wang, and Z. Feng, "Low-PAPR integrated sensing and communication waveform design," *IEEE WCNC*, Glasgow, United Kingdom, 2023, pp. 1-6.

[44] Y. Huang, S. Hu, S. Ma, Z. Liu, and M. Xiao, "Designing low-PAPR waveform for OFDM-based RadCom systems," *IEEE Trans. Wireless Commun.*, vol. 21, no. 9, pp. 6979-6993, Sept. 2022.

[45] P. Varshney, P. Babu, and P. Stoica, "Low-PAPR OFDM waveform design for radar and communication systems," *IEEE Trans. Radar Syst.*, vol. 1, pp. 69-74, May 2023.

[46] J. Wu, L. Li, W. Lin, J. Liang, and Z. Han, "Low-complexity waveform design for PAPR reduction in integrated sensing and communication systems based on ADMM," *IEEE Sens. J.*, vol. 24, no. 11, pp. 18488-18498, Jun. 2024.

[47] J. Wu, L. Li, W. Lin, J. Liang, and Z. Han, "ADMM-based Low-PAPR OFDM waveform design for dual-functional radar-communication systems," *IEEE ICC*, Denver, USA, 2024, pp. 305-310.

[48] L. Tsai, W. Chung, and D. Shiu, "Synthesizing low autocorrelation and low PAPR OFDM sequences under spectral constraints through convex optimization and GS algorithm," *IEEE Trans. Signal Process.*, vol. 59, no. 5, pp. 2234-2243, May 2011.

[49] E. Ghadimi, A. Teixeira, I. Shames, and M. Johansson, "Optimal parameter selection for the alternating direction method of multipliers (ADMM): Quadratic problems," *IEEE Trans. Autom. Control*, vol. 60, no. 3, pp. 644-658, Mar. 2015.

[50] M. Richards and W. Melvin, *Principles of modern radar: Basic principles*, North Carolina, SciTech Publishing, 2023.

[51] W. Melvin, "Space-time adaptive radar performance in heterogeneous clutter," *IEEE Trans. Aerosp. Electron. Syst.*, vol. 36, no. 2, pp. 621-633, Apr. 2000.